Article

Cell

UBQLN4 Represses Homologous Recombination and Is Overexpressed in Aggressive Tumors

Graphical Abstract

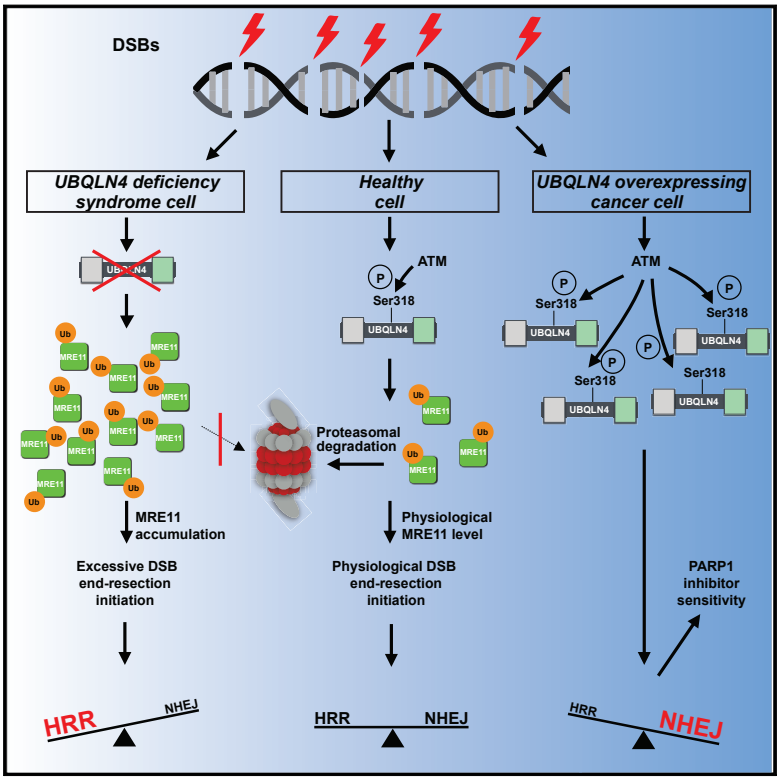

Highlights

- Homozygous *UBQLN4* germline mutations lead to a genome instability syndrome
- UBQLN4 removes ubiquitylated MRE11 from damaged chromatin to curtail DSB resection
- UBQLN4 overexpression represses HRR and promotes the use of NHEJ for DSB repair
- UBQLN4 overexpression in tumors promotes PARP1 inhibitor sensitivity

Authors

Ron D. Jachimowicz, Filippo Beleggia, Jörg Isensee, ..., H. Christian Reinhardt, Dagmar Wieczorek, Yosef Shiloh

Correspondence

ron.jachimowicz@uk-koeln.de (R.D.J.), yaelz@post.tau.ac.il (Y.Z.), christian.reinhardt@uk-koeln.de (H.C.R.), dagmar.wieczorek@hhu.de (D.W.), yossih@post.tau.ac.il (Y.S.)

In Brief

Control of MRE11 association with chromatin by UBQLN4 during double-strand break repair influences repair pathway choice and can be dysregulated in tumorigenesis.

Jachimowicz et al., 2019, Cell *176*, 505–519
January 24, 2019
https://doi.org/10.1016/j.cell.2018.11.024

CellPress

Cell

UBQLN4 Represses Homologous Recombination and Is Overexpressed in Aggressive Tumors

Ron D. Jachimowicz,[1,2,3,*] Filippo Beleggia,[3,5,18] Jörg Isensee,[6,18] Bhagya Bhavana Velpula,[1,2,18] Jonas Goergens,[3] Matias A. Bustos,[7] Markus A. Doll,[4,8] Anjana Shenoy,[2] Cintia Checa-Rodriguez,[9] Janica Lea Wiederstein,[4] Keren Baranes-Bachar,[1,2] Christoph Bartenhagen,[10,11] Falk Hertwig,[12,13,14] Nizan Teper,[1,2] Tomohiko Nishi,[7] Anna Schmitt,[3] Felix Distelmaier,[15] Hermann-Josef Lüdecke,[5,16] Beate Albrecht,[16] Marcus Krüger,[4,11] Björn Schumacher,[4,8] Tamar Geiger,[2] Dave S.B. Hoon,[7] Pablo Huertas,[9] Matthias Fischer,[10,11] Tim Hucho,[6] Martin Peifer,[11,17] Yael Ziv,[1,2,19,*] H. Christian Reinhardt,[3,4,11,19,20,*] Dagmar Wieczorek,[5,16,19,*] and Yosef Shiloh[1,2,19,*]

[1]The David and Inez Myers Laboratory for Cancer Genetics, Sackler School of Medicine, Tel Aviv University, Tel Aviv 69978, Israel
[2]Department of Human Molecular Genetics and Biochemistry, Sackler School of Medicine, Tel Aviv University, Tel Aviv 69978, Israel
[3]Clinic I of Internal Medicine, University Hospital Cologne, Cologne 50931, Germany
[4]Cologne Excellence Cluster on Cellular Stress Response in Aging-Associated Diseases, University of Cologne, Cologne, Germany
[5]Institute of Human Genetics, Heinrich-Heine-University, Düsseldorf, Germany
[6]Department of Anesthesiology and Intensive Care Medicine, Experimental Anesthesiology and Pain Research, University Hospital Cologne, Cologne 50931, Germany
[7]Department of Translational Molecular Medicine, Division of Molecular Oncology, John Wayne Cancer Institute at Providence Saint John's Health Center, Santa Monica, CA, USA
[8]Institute for Genome Stability in Aging, Cologne, Germany
[9]Centro Andaluz de Biología Molecular y Medicina Regenerativa-CABIMER, Universidad de Sevilla-CSIC-Universidad Pablo de Olavide and Department of Genetics, University of Sevilla, Sevilla 41092, Spain
[10]Department of Experimental Pediatric Oncology, University Hospital Cologne, Cologne, Germany
[11]Center for Molecular Medicine Cologne, University of Cologne, Cologne, Germany
[12]Department of Pediatric Oncology and Hematology, Charité, Berlin, Germany
[13]German Cancer Consortium, Germany
[14]Berlin Institute of Health, Germany
[15]Department of General Pediatrics, Neonatology and Pediatric Cardiology, University Hospital, Heinrich-Heine-University, Düsseldorf 40225, Germany
[16]Institute of Human Genetics, University Clinic Duisburg-Essen, Essen, Germany
[17]Department of Translational Genomics, University of Cologne, Cologne, Germany
[18]These authors contributed equally
[19]These authors contributed equally
[20]Lead contact
*Correspondence: ron.jachimowicz@uk-koeln.de (R.D.J.), yaelz@post.tau.ac.il (Y.Z.), christian.reinhardt@uk-koeln.de (H.C.R.), dagmar.wieczorek@hhu.de (D.W.), yossih@post.tau.ac.il (Y.S.)
https://doi.org/10.1016/j.cell.2018.11.024

SUMMARY

Genomic instability can be a hallmark of both human genetic disease and cancer. We identify a deleterious *UBQLN4* mutation in families with an autosomal recessive syndrome reminiscent of genome instability disorders. UBQLN4 deficiency leads to increased sensitivity to genotoxic stress and delayed DNA double-strand break (DSB) repair. The proteasomal shuttle factor UBQLN4 is phosphorylated by ATM and interacts with ubiquitylated MRE11 to mediate early steps of homologous recombination-mediated DSB repair (HRR). Loss of UBQLN4 leads to chromatin retention of MRE11, promoting non-physiological HRR activity *in vitro* and *in vivo*. Conversely, UBQLN4 overexpression represses HRR and favors non-homologous end joining. Moreover, we find UBQLN4 overexpressed in aggressive tumors. In line with an HRR defect in these tumors, UBQLN4 overexpression is associated with PARP1 inhibitor sensitivity. UBQLN4 therefore curtails HRR activity through removal of MRE11 from damaged chromatin and thus offers a therapeutic window for PARP1 inhibitor treatment in UBQLN4-overexpressing tumors.

INTRODUCTION

In response to genotoxic stress, cells activate a signaling network, collectively referred to as the DNA damage response (DDR). The DDR activates cell-cycle checkpoints, DNA repair pathways, and, if damage is beyond repair capacity, triggers cell-death pathways (Reinhardt and Yaffe, 2013). Following DNA double-strand breaks (DSBs), the DDR is primarily activated by the proximal kinase ataxia telangiectasia mutated (ATM), which phosphorylates a plethora of substrates, such as KAP-1, CHK2, p53, MRE11, RAD50, NBS1, and others (Shiloh and Ziv, 2013).

The main DSB repair pathways are the canonical non-homologous end joining (c-NHEJ) pathway and homologous

recombination repair (HRR). Error-prone c-NHEJ operates throughout the cell cycle and directly ligates the processed DSB ends, whereas error-free HRR is restricted to late S and G_2, when a repair template is available (Dietlein et al., 2014). Additional mutagenic DSB repair pathways are alternative NHEJ and single-strand annealing (Dietlein et al., 2014). The balance between these different pathways is essential for correct DSB repair (Dietlein et al., 2014).

In contrast to the wealth of phosphorylation targets in the DDR, the number of known ubiquitylation substrates at DSB sites is small (Harding and Greenberg, 2016). While K63-linked ubiquitylation mediates functional alterations of the target protein, K48-linked ubiquitin chains mark target proteins for proteasome-mediated degradation (Walczak et al., 2012). Notably, we previously observed recruitment of proteasomes to DSB sites (Levy-Barda et al., 2011), raising the possibility that the regulated turnover of proteins at DSB sites may be critical for a proper DSB response.

In proteasome-mediated protein degradation, ubiquitylated proteins are recognized by specific proteasome subunits (Grice and Nathan, 2016). Additional selectivity is provided by loosely associated shuttle factors that mediate target recognition by the proteasome. Three such shuttles were identified in budding yeast: Dsk2, Rad23, and Ddi1 (Hartmann-Petersen et al., 2003). Rad23 and Ddi1 have been implicated in the DDR, as Rad23 functions in nucleotide excision repair (Ng et al., 2003), and Ddi1 is required in the proteasomal degradation of homothallic switching (HO) endonuclease, which generates a site-specific DSB at the mating type locus (Kaplun et al., 2005). The mammalian orthologs of Dsk2 are members of the ubiquilin family, ubiquilin1–4 (UBQLN1–4) (Hu et al., 2012). Ubiquilins contain ubiquitin-like (UBL) and ubiquitin-binding (UBA) domains. Their role as shuttles that direct cargo to the proteasome is mediated by the binding of ubiquitylated proteins through their UBA domain and simultaneous interaction with the proteasome subunit s5a through their UBL domain (Ko et al., 2004).

Here, we identify a homozygous *UBQLN4* germline mutation, p.R326X, in a complex inherited disorder. Affected patients display characteristics similar to other genome instability syndromes, such as ataxia-telangiectasia and others (Hoeijmakers, 2001). Mechanistically, we show that UBQLN4 is phosphorylated in an ATM-dependent manner and recruited to sites of DNA damage, where it redirects DSB repair toward NHEJ by functionally repressing HRR. We further show that UBQLN4 interacts with ubiquitylated MRE11, to facilitate its proteasomal degradation. Moreover, reduced HRR usage in *UBQLN4*-overexpressing tumor cells is associated with an actionable PARP1 inhibitor sensitivity.

RESULTS

Identification of the UBQLN4 Deficiency Syndrome

We identified an autosomal recessive syndrome in two consanguineous families (Figures 1A and 1B). Two patients (*A-IV-4*, *B-IV-3*) were followed from birth to 10 and 11 years of age, respectively. Patient *A-IV-3* was a stillbirth and was hence not followed further. These patients displayed intellectual impairment, growth retardation, microcephaly, facial dysmorphism, hearing loss, ataxia, and anemia. Moreover, a pregnancy in family *A* was terminated at the end of the first trimester due to polyhydramnios, nuchal translucency, and single umbilical artery (fetus *A-IV-5*). A detailed clinical description of the patients is provided in Figures 1A, 1B, and S2 and Table S1 and the Human subjects section within the STAR Methods. We performed whole-exome sequencing of cells isolated from *A-IV-4* and *A-IV-5*. This analysis revealed a detrimental homozygous c.976C > T mutation in exon 6 of the *UBQLN4* gene in both patients (Figure S1A; Table S2). This mutation is predicted to create a premature stop codon (p.R326X) (Figure 1C). Sanger sequencing confirmed c.976C > T homozygosity in the affected individuals, while the parents were heterozygous carriers (Figures 1C and S1B). Of note, out of a total of 8 shared homozygous variants, the *UBQLN4* c.976C > T mutation was the only shared aberration predicted to be truncating (Figure S1A; Table S2).

To investigate whether the c.976C > T mutation affects UBQLN4 expression, we performed immunoblots. We analyzed dermal fibroblasts (DMFs) derived from *B-IV-3*, *A-IV-5*, and *B-III-2* using antibodies directed against C- and N-terminal UBQLN4 epitopes. Neither of these antibodies detected full-length UBQLN4 in cells from *B-IV-3* or *A-IV-5*, while DMFs derived from *B-III-2* showed reduced UBQLN4 expression, compared to wild-type (WT) (Figures 1D and S1C). We note that the N-terminal antibody detected a faint unspecific band in WT cells below the full-length UBQLN4 band that was also seen in patient-derived cells (Figure S1C). To rule out the possibility of a transcript variant that skips the c.976C > T mutation in exon 6, we performed RNA sequencing (RNA-seq). The expressed allelic fraction of the p.R326X mutation was 100% in both patients (Figure 1E). In addition, *A-IV-5* and *B-IV-3* showed a low-level expression of a novel transcript containing an exon 5–7 splice junction, omitting exon 6 (Figure 1E). However, exon 6 skipping leads to a frameshifted transcript, predicted to contain a downstream stop codon (p.L321X), potentially giving rise to a 321-amino-acid protein, which was not detected in patient cells (Figure 1D). Of note, patient cells, and to a lesser extent parent cells, showed on average an almost 3-fold decrease in *UBQLN4* mRNA expression, compared to WT samples of the same cell type (Figure S1D), indicating that the mutant transcripts may be subject to nonsense-mediated mRNA decay. Our data indicate that the c.976C > T mutation creates a *UBQLN4*-null allele, leading to a novel autosomal recessive syndrome in homozygotes, which we term "UBQLN4 deficiency syndrome."

Loss of UBQLN4 Confers Hypersensitivity to Genotoxic Agents

We recently conducted an RNAi screen in conjunction with automated microscopy, using ATM-dependent KAP-1 phosphorylation as a readout (Figure S1E) (Baranes-Bachar et al., 2018). Re-analysis of these experiments revealed sustained KAP-1 phosphorylation in UBQLN4-depleted cells after treatment with the radiomimetic drug neocarzinostatin (NCS), suggesting delayed DNA repair in the absence of UBQLN4 (Figure S1F). Thus, we next examined the response of cells derived from patient *B-IV-3* to genotoxic stress. Patient and

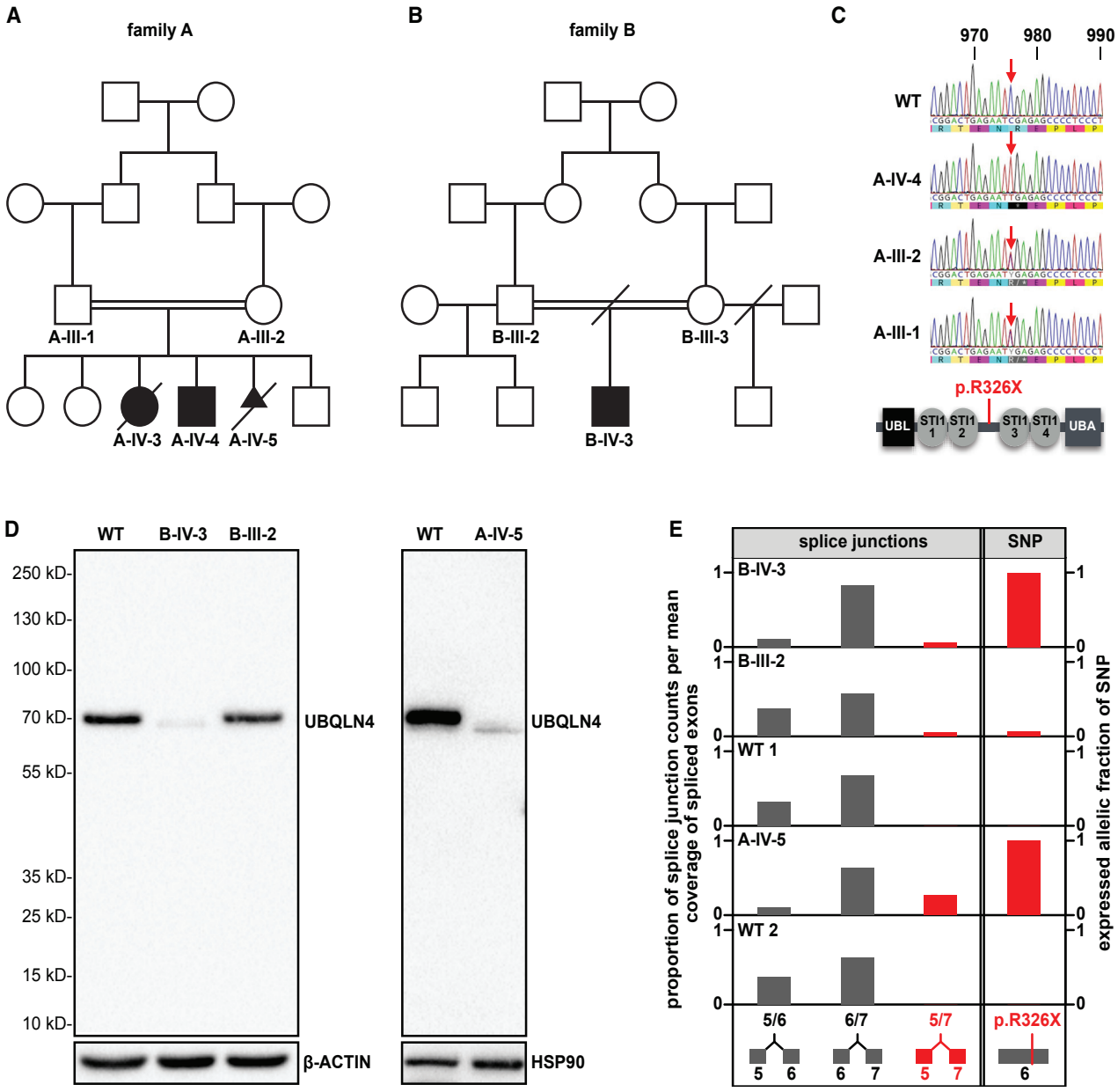

Figure 1. A Homozygous c.976C > T Mutation in the *UBQLN4* Gene Leads to UBQLN4 Deficiency Syndrome

(A) Pedigree of UBQLN4 deficiency syndrome in family A.

(B) Pedigree of UBQLN4 deficiency syndrome in family B.

(C) Sequencing of lymphocyte gDNA from a healthy donor (WT), *A-IV-4* and his parents. Arrow indicates the c.976C > T mutation. Bottom: domain diagram of UBQLN4 depicting the N-terminal UBL, C-terminal UBA domain, and 4 middle-region STI1 motifs. The p.R326X mutation is indicated.

(D) Immunoblot detecting UBQLN4 in the DMF lines with an antibody against the C-terminal epitope.

(E) Proportion of splice junction counts per mean coverage of spliced exons and expressed allelic fraction of the c.976C > T mutation obtained from RNA-seq of *A-IV-4*, *B-IV-3*, *B-III-2*, and 2 WT controls.

See also Figures S1 and S2 and Tables S1 and S2.

WT DMFs were treated with NCS, etoposide, cisplatin, or hydroxyurea (HU). Consistent with a role of UBQLN4 in the DDR, *UBQLN4* mutant cells exhibited a significantly increased sensitivity to all four genotoxic agents, compared to WT (Figures 2A–2D). Heterozygous cells showed NCS, etoposide, and HU sensitivities, between those of patient and WT cells (Figures 2A, 2B, and 2D). Cisplatin sensitivity was similar in the patient and heterozygous cells (Figure 2C). Complementation of patient cells with UBQLN4^{wt} reverted the hypersensitivity to all four genotoxic agents (Figures S3A–S3E). Furthermore, RNAi-mediated

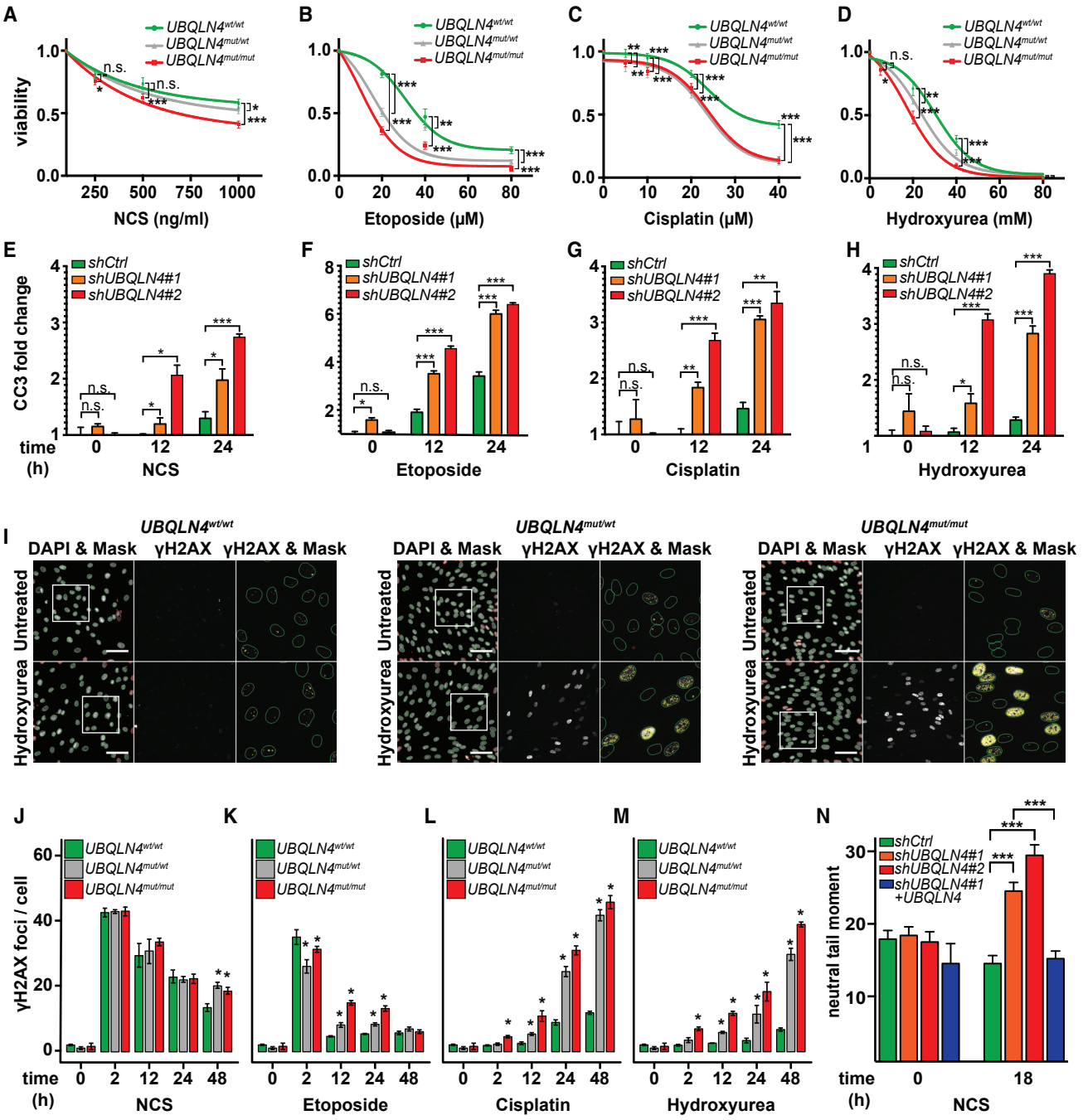

Figure 2. UBQLN4 Loss Increases Cellular Sensitivity to Genotoxic Agents

(A–D) Cells of the indicated genotypes were treated with NCS (A), etoposide (B), cisplatin (C), or HU (D) for 96 hr and viability was assessed by CellTiterGlo assays. Error bars represent SD of the mean of 3 independent experiments. p values were calculated using t test with Welch's correction not assuming equal variance. *p < 0.05, **p < 0.01, ***p < 0.001.

(E–H) Cleaved caspase-3 positivity was assessed by flow cytometry at the indicated time points in U2OS cells transduced with the indicated constructs, after NCS (500 ng/mL) (E), etoposide (10 μM) (F), cisplatin (20 μM) (G), or HU (20 mM) (H) treatment. Error bars represent SD of the mean of n = 3 experiments. Significance was determined with paired Student's t test. *p < 0.05, **p < 0.01, ***p < 0.001.

(I) Representative images of γH2AX foci 48 hr after HU (20 mM) or mock treatment, using HCS microscopy. DAPI served as a counterstain. Scale bars, 100 μm.

(J–M) Cells of the indicated genotypes were treated for 2 hr with NCS (500 ng/mL) (J), etoposide (20 μM) (K), cisplatin (20 μM) (L), or HU (20 mM) (M) and stained for γH2AX at the indicated time points. Data were analyzed with R, using ordinary two-way ANOVA. Bonferroni post hoc analysis was applied to determine p values

(legend continued on next page)

UBQLN4 depletion rendered U2OS cells significantly more sensitive against NCS, compared to controls in clonogenic survival assays (Figures S3F and S3G). Of note, ATM inhibition with KU60019 had a slightly more pronounced effect on NCS sensitization than UBQLN4 depletion (Figures S3F and S3G). Next, we quantified DNA damage-induced apoptosis in U2OS cells expressing either two distinct UBQLN4-depleting short hairpin RNAs (shRNAs), or a control hairpin (Figure S3F). When cells were treated with NCS, etoposide, cisplatin, or HU, UBQLN4-depleted cells displayed a significantly increased cleaved-caspase-3 (CC3)-positive population in response to all four genotoxic agents, compared to controls (Figures 2E–2H). These results suggest that loss of UBQLN4 confers hypersensitivity to DNA-damaging agents and leads to enhanced apoptotic cell death in response to DNA damage.

UBQLN4 Depletion Results in Impaired DSB Repair

To ask whether *UBQLN4* loss of function affects DNA repair kinetics, we next assessed the accumulation and clearance of DNA lesions in DMFs following NCS, etoposide, cisplatin, or HU exposure. We employed automated immunofluorescence microscopy to quantify nuclear γH2AX foci, as a surrogate for unrepaired DNA lesions (Figures 2I–2M). In response to NCS and etoposide, we observed a significantly delayed clearance of γH2AX foci in patient and heterozygous cells, compared to WT (Figures 2J and 2K). Of note, UBQLN4 depletion in U2OS cells resulted in a similarly delayed clearance of NCS-induced γH2AX foci, compared to controls (Figure S3H). In contrast to the etoposide and NCS response, cells treated with cisplatin and HU showed a continuous increase of γH2AX foci throughout the 48-hr observation period (Figures 2L–2M). In line with defective DNA repair in UBQLN4-deficient settings, patient and heterozygous cells displayed a significantly increased number of γH2AX foci following cisplatin and HU exposure, compared to WT (Figures 2L–2M). We observed a massive accumulation of γH2AX foci in late S-phase, specifically in cisplatin-treated *UBQLN4* mutant cells, compared to WT (Figure S3I). Moreover, the decrease in cell counts induced by each of the genotoxic agents was significantly enhanced in patient cells, and to a lesser extent in heterozygous cells, compared to WT (Figure S3J). In line with the experiments shown in Figure S3B, re-expression of ectopic *UBQLN4* rescued the number of surviving *UBQLN4* mutant cells after NCS treatment (Figure S3K).

To determine the impact of UBQLN4 depletion on the sealing of NCS-induced DSBs, we performed neutral comet assays in U2OS cells expressing two distinct *UBQLN4*-targeting shRNAs or a control shRNA. Of note, alkaline comet assays do not differentiate between single-strand break and DSB, whereas the neutral comet assay specifically reports DSBs (Olive and Banáth, 2006). The comet assays revealed a substantial DSB repair defect in *UBQLN4*-depleted cells, which could be rescued upon re-expression of shRNA-resistant $UBQLN4^{wt}$ (Figures 2N and S3L–S3M).

UBQLN4 Is Recruited to Sites of DNA Damage

To ask whether UBQLN4 relocates to sites of DNA lesions, we induced focal DNA damage by micro-laser irradiation of single nuclei in U2OS cells. Using an UBQLN4-specific antibody (Figures S3N and S3O), we noticed that UBQLN4 was recruited to these sites, where it co-localized with 53BP1 (Figure 3A). To further characterize the kinetics of this UBQLN4 recruitment, we expressed ectopic GFP.UBQLN4 in U2OS cells and monitored its recruitment to laser-induced damage. A fraction of GFP.UBQLN4 was recruited to the damage sites within 5 min of damage induction (Figure 3B). We also employed biochemical fractionation to demonstrate enrichment of UBQLN4 in the chromatin fraction after NCS exposure (Figure S4A). To assess whether the UBL or UBA domains of UBQLN4 were required for this recruitment, we generated UBQLN4 deletion mutants (Figure S4B) and found that neither the UBL nor the UBA domain was required for recruitment to sites of laser-induced damage (Figure S4C).

ATM-Dependent UBQLN4 Phosphorylation Is Required for a Proper Cellular DDR

A phosphoproteomic screen previously detected a peptide that represented phosphorylation of UBQLN4 on S318 in response to ionizing radiation (IR) (Matsuoka et al., 2007). Importantly, S318 is located in a highly conserved S-S-Q-P amino acid sequence that contains the potential ATM substrate motif, S^{318}-Q (Reinhardt and Yaffe, 2013) (Figure 3C). We therefore aimed to validate this finding and to further characterize the regulation and functional significance of this phosphorylation. We raised a polyclonal, phospho-specific antibody against pS318/UBQLN4 and assessed its specificity in anti-GFP immunoprecipitates from IR-treated U2OS cells overexpressing GFP.UBQLN4 or a non-phosphorylatable $GFP.UBQLN4^{S318A}$ mutant. The anti-pS318 UBQLN4 signal was enhanced following IR in $UBQLN4^{wt}$, compared to $GFP.UBQLN4^{S318A}$ precipitates (Figures S4D and S4E). When we inspected the anti-GFP precipitates on SDS-PAGE, we also detected endogenous UBQLN4, indicating the formation of homo-dimers or -polymers, an observation that we confirmed in co-immunoprecipitation experiments (Figures S4D and S4F). The signal obtained with the anti-pS318 antibody in immunoblotting of lysates from irradiated cells was reduced when the cells were UBQLN4 depleted (Figure S4G). Notably, pS318/UBQLN4 was induced by several genotoxic agents, including IR, etoposide, camptothecin, and HU (Figures S4H and S4I). Moreover, pS318/UBQLN4 was detected primarily in the nuclear and particularly the chromatin fraction, whereas only faint signals were obtained in cytoplasmic and membrane fractions (Figure S4J). Longitudinal monitoring revealed that pS318/UBQLN4 peaked within 30 min after IR and subsided 4–6 hr later (Figure 3D). These kinetics are similar to that of ATM-mediated KAP-1 phosphorylation (Figure 3D). As the S-Q motif can similarly be phosphorylated by other kinases, such

of selected pairs defined in a contrast matrix using the R library multcomp. Error bars represent SD of the mean for 3 replicate wells analyzed in one experiment. Each experiment was carried out twice. *$p < 0.05$.

(N) Quantification of the relative comet tail moment (n = 100) derived from the neutral comet assays at the indicated time points. Error bars represent SD of the mean of the relative comet tail moment analyzed in n = 3 experiments. Significance was determined with paired Student's t test. *$p < 0.05$, **$p < 0.01$, ***$p < 0.001$. See also Figure S3.

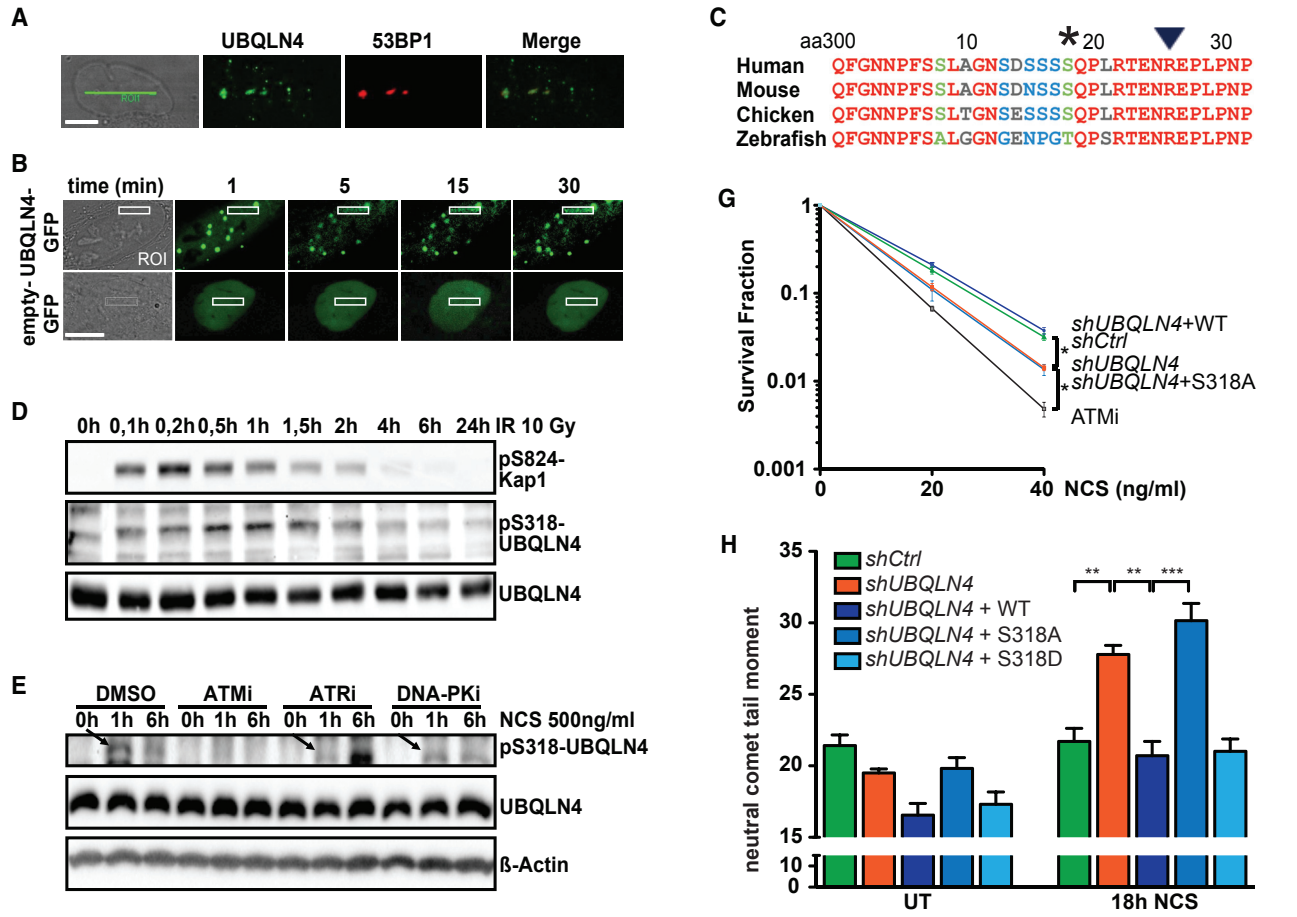

(legend on next page)

as ataxia telangiectasia- and Rad3-related (ATR) and DNA dependent protein kinase (DNA-PK) (Reinhardt and Yaffe, 2013), we employed small-molecule inhibitors to examine their role in this phosphorylation. Consistent with an ATM dominance in mediating S318/UBQLN4 phosphorylation, the ATM inhibitor, KU60019, abolished NCS-induced pS318/UBQLN4. The ATR inhibitor, AZ20, appeared to delay this phosphorylation, whereas the DNA-PK inhibitor, KU60648, had no apparent effect on S318 phosphorylation (Figures 3E and S4K). We validated the ATM dependence of the S318 phosphorylation in a phospho-mass spectrometry experiment (Figure 3F; Table S3). We treated FLAG.UBQLN4-expressing U2OS cells with NCS (1 hr, 500 ng/mL) or vehicle. To assess the role of ATM in UBQLN4 phosphorylation, we also included cells that were treated with KU60019 30 min prior to addition of NCS. We found 1,400 NCS-induced phosphorylation sites, of which 522 were less abundant in the presence of KU60019 (Table S3). Importantly, NCS treatment induced S318 phosphorylation, which was almost completely abolished in the presence of KU60019 (Figure 3F). Of note, the pS144/UBQLN4 site displayed a similar ATM-dependent and NCS-induced phosphorylation pattern (Figure S4L), indicating that UBQLN4 is also targeted by kinase(s), selecting proline-directed motifs.

To ask whether UBQLN4 phosphorylation impacts on sensitivity to genotoxic stress, we used clonogenic survival assays in U2OS cells (Figures 3G and S4M). UBQLN4 depletion resulted in marked NCS sensitivity, compared to control cells (Figure 3G). This phenotype could be fully rescued by ectopic expression of UBQLN4^{wt}, whereas UBQLN4^{S318A} failed to rescue the UBQLN4 depletion phenotype, similar to UBQLN4 mutant proteins lacking either the UBL or UBA domain (Figures 3G, S4N, and S4O). We next tested whether UBQLN4 phosphorylation interferes with the sealing of NCS-induced DSBs, using a neutral comet assay carried out in the cell clones used in Figure 3G, as well as a UBQLN4-depleted clone that was complemented with a phospho-mimicking S318D mutant (Figure S4P). Here, UBQLN4 depletion significantly delayed DSB sealing, compared to cells expressing control shRNA or UBQLN4-depleted cells that were complemented with either WT or UBQLN4^{S318D} (Figures 3H and S4Q). UBQLN4-depleted cells complemented with UBQLN4^{S318A} displayed a comet tail moment that was indistinguishable from that observed in UBQLN4-depleted cells (Figures 3H and S4Q). These results suggest that UBQLN4 phosphorylation on S318 is functionally important for its role in the DSB response.

Loss of UBQLN4 Leads to Increased HRR

Mammalian cells employ two major DSB repair pathways, namely, NHEJ and HRR (Dietlein et al., 2014). Particularly HRR is dependent on ATM activity (Dietlein et al., 2014). Here, we showed that UBQLN4 is an ATM substrate and that DSB sealing is markedly impaired in UBQLN4-depleted cells. HRR depends on a 5′-3′ DSB end resection, which is initiated by the MRE11 nuclease (Symington and Gautier, 2011). As UBQLN4 is a proteasome shuttling factor (Ko et al., 2004), we next pursued a candidate approach to ask whether UBQLN4 interacts with HRR proteins. We treated GFP- and GFP.UBQLN4-expressing U2OS cells with vehicle solution or NCS and performed anti-GFP pull-downs, which revealed that MRE11 co-precipitated with GFP.UBQLN4, particularly after NCS exposure (Figure S5A). These data suggest that MRE11 is one of probably many UBQLN4 interaction partners. Based on this observation, we hypothesized that UBQLN4 might direct DSB repair pathway choice. Thus, we used two distinct assays to assess the differential use of HRR and NHEJ in UBQLN4-depleted and UBQLN4-overexpressing U2OS cells. Using the SeeSaw reporter system (López-Saavedra et al., 2016) to quantify the relative use of HRR and NHEJ, we found that UBQLN4 depletion significantly increased the relative contribution of HRR over NHEJ in DSB repair, whereas UBQLN4 overexpression significantly increased the relative use of NHEJ (Figures 4A and S5B). Of note, expression of UBQLN4^{S318A} failed to promote NHEJ (Figure 4A).

We corroborated these data using the DR-GFP reporter (López-Saavedra et al., 2016) (Figure S5C). Similar to the SeeSaw system, the DR-GFP assay demonstrated significantly increased HRR usage in UBQLN4-depleted cells, compared to controls (Figure 4B). UBQLN4-overexpressing cells showed significantly decreased HRR usage, whereas expression of UBQLN4^{S318A} had no detectable impact on HRR usage (Figure 4B).

Figure 3. The ATM Target UBQLN4 Localizes to Sites of DNA Damage

(A) Recruitment of endogenous UBQLN4 to sites of laser-induced damage. Cells were laser microirradiated and stained 15 min later for UBQLN4 and 53BP1. The green line (left panel) indicates the location of laser-induced damage. Scale bar, 10 μm.

(B) Dynamics of UBQLN4-recruitment to laser-induced DNA damage. Cells were depleted of endogenous UBQLN4 (3′ UTR-targeting shRNA) and complemented with GFP or UBQLN4.GFP. Scale bar, 10 μm.

(C) Sequence alignment within *UBQLN4* exon 6 depicting inter-species conservation. Asterisk indicates *Homo sapiens* S318. Triangle indicates the p.R326X mutation.

(D) Immunoblot displaying the time course of the S318 UBQLN4 phosphorylation in U2OS cells after 10 Gy IR.

(E) UBQLN4 phosphorylation is ATM mediated. U2OS cells were treated with the indicated inhibitors 30 min prior to NCS (500 ng/mL, 1 hr) exposure and subsequent immunoblotting. Arrows indicate pS318/UBQLN4 bands. ATMi, KU60019 (5 μM); DNA-PKi, KU60648 (10 μM); ATRi, AZ20 (0.5 μM).

(F) Selected LC-MS/MS scan of the pS318/UBQLN4 peptide and annotated b- and y-ions. Fragment ions marked with asterisk result from loss of the phospho-group. Inset top right: LC-MS/MS measured intensities of the pS318 site after indicated treatments.

(G) Clonogenic survival assay of U2OS cells transfected with the indicated constructs and treated with the indicated NCS concentrations. Cells transfected with *shUBQLN4* or pre-treated with KU60019 served as controls. Error bars represent SD of the mean of n = 3 experiments. p values were calculated using the t test with Welch's correction not assuming equal variance. *$p < 0.05$.

(H) Quantification of the relative comet tail moment on the indicated cells (n = 100) was assessed, using an automated COMET analysis software package. Error bars represent SD of the mean of the relative comet tail moment analyzed in n = 3 experiments. Significance was determined with paired Student's t test. *$p < 0.05$, **$p < 0.01$, ***$p < 0.001$.

See also Figure S4 and Table S3.

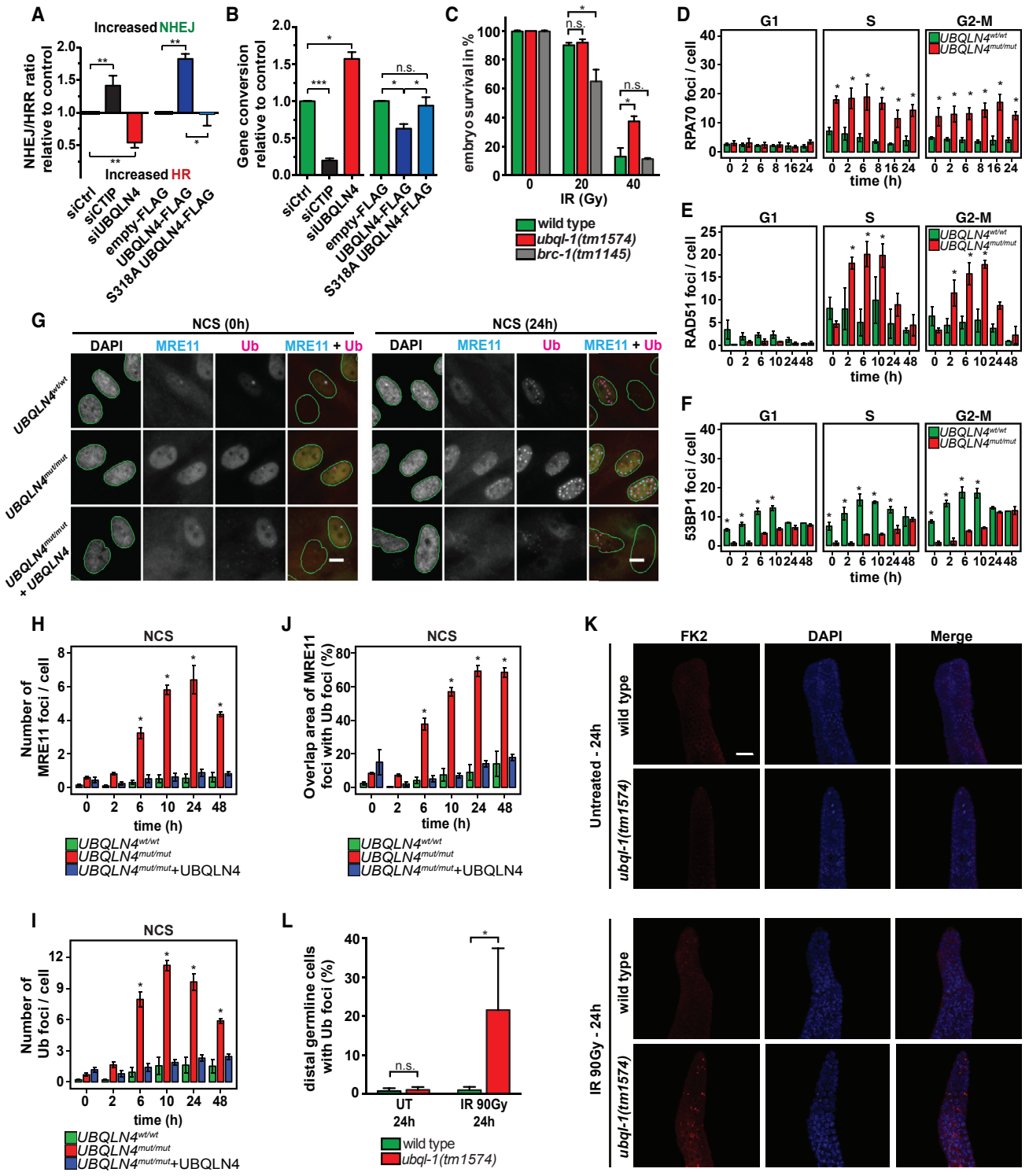

Figure 4. Loss of UBQLN4 Leads to Increased HRR

(A) Effect of UBQLN4 small interfering RNA (siRNA), FLAG.UBQLN4 or FLAG.UBQLN4^{S318A} overexpression on the NHEJ:HRR ratio in the SeeSaw reporter assay. CTIP-depleting siRNAs served as a positive control. Irrelevant siRNA and FLAG plasmid served as controls. An NHEJ:HRR ratio >1.0 represents a shift toward NHEJ. The data represent 4 sets of triplicate experiments. Error bars represent SEM. A paired t test was used for statistical analysis. *$p < 0.05$, **$p < 0.01$.

(legend continued on next page)

We validated these findings *in vivo*, by assessing the role of *C. elegans ubql-1*, the nematode ortholog of *UBQLN4*, in HRR. During the first hours of embryogenesis, *C. elegans* selectively employs HRR to repair DSBs (Lemmens and Tijsterman, 2011). IR of early WT *C. elegans* embryos led to a dose-dependent survival reduction, which was significantly alleviated in the *ubql-1* mutant (Figure 4C). These data imply an evolutionarily conserved role for *UBQLN4* in DSB repair.

Our data may suggest a model in which UBQLN4 regulates DSB repair pathway choice by repressing HRR through removal of HRR factors from the damaged site. We tested this model by comparing the NCS-induced spatial dynamics of several HRR factors in *UBQLN4* mutant and WT cells. We longitudinally monitored RPA70 and RAD51 foci (indicators of ongoing HRR), as well as 53BP1 foci (indicating NHEJ activity) (Dietlein et al., 2014) and observed a significantly increased number of RPA70 and RAD51 foci in patient cells, compared to WT (Figures 4D and 4E). This difference was particularly obvious in S-phase and G_2/M cells (Figures 4D and 4E). In contrast, 53BP1 foci were significantly reduced in NCS-treated patient cells, compared to controls (Figure 4F), supporting a role of UBQLN4 in curtailing HRR. To rule out a net effect of the different amounts of DNA lesions in the different genotypes (Figure 2J), we normalized the number of RPA70 and 53BP1 foci against amounts of γH2AX foci (representing unrepaired DSBs) (Figures S5D and S5E). The results indicated that the increased RPA70 and decreased 53BP1 foci in *UBQLN4* mutant cells were not the result of an increased number of unrepaired DNA lesions *per se* (Figures S5D and S5E).

UBQLN4 Is Required for MRE11 Turnover in the Chromatin

We showed that the DSB resection-initiating nuclease MRE11 interacts with UBQLN4 in response to NCS (Figure S5A). To scrutinize the role of the UBQLN4:MRE11 interaction for DSB repair, we examined the effect of UBQLN4 depletion on MRE11 retention in the damaged chromatin (Figures S5F and S5G). We carried out cycloheximide chase experiments in conjunction with NCS treatment in WT and *UBQLN4* mutant cells. These experiments revealed a significantly increased accumulation of MRE11 in the chromatin fraction of *UBQLN4* mutant cells, compared to WT, 6 hr after NCS treatment (Figures S5F and S5G). This observation was validated using longitudinal immunofluorescence. As shown in Figures 4G and 4H, MRE11 nuclear foci were significantly increased in *UBQLN4* mutant DMFs 6–48 hr after NCS treatment, compared to WT and UBQLN4^{wt}-complemented patient cells. Of note, the cell-cycle distribution of untreated and NCS-exposed WT, *UBQLN4* mutant, and UBQLN4^{wt}-complemented patient cells showed only mild differences (Figure S5H). Specifically, WT cells showed slightly increased S-phase and G_2 populations, compared to *UBQLN4* mutant cells (Figure S5H), which, if anything, should lead to an underestimation of the increased HRR in *UBQLN4* mutant cells.

To ask whether UBQLN4-deficient cells accumulate ubiquitylated proteins at DNA damage sites, we performed immunofluorescence with the FK2 antibody, to detect mono- and polyubiquitylated proteins. *UBQLN4* mutant cells showed increased numbers of FK2-positive nuclear foci after NCS exposure, compared to WT or patient cells complemented with UBQLN4^{wt} (Figures 4G and 4I). Pre-treatment with the proteasome inhibitor MG132 led to similar amounts of NCS-induced FK2 foci in patient and WT cells (Figure S5I), indicating that the NCS-induced FK2 foci in patient cells result primarily from inefficient proteasomal clearance of ubiquitylated proteins from damage sites. Intriguingly, the overlap area of MRE11 and FK2 foci was markedly increased in patient cells, compared to WT and UBQLN4-complemented patient cells, potentially indicating that MRE11 is ubiquitylated itself and accumulates at DSB sites in patient cells (Figures 4G and 4J). We obtained similar data in *ubql-1* mutant *C. elegans*. IR treatment induced massive accumulation of FK2 foci after 24 hr in the distal germline of *ubql-1* mutant worms, compared to WT animals (Figures 4K and 4L).

(B) Cells harboring a single copy of DR-GFP were transfected with the indicated siRNAs or FLAG plasmids and gene conversion was assessed. Non-target siRNA and FLAG plasmid served as controls. siRNA against CTIP was used as a positive control. The data represent 4 sets of triplicate experiments. Error bars represent SEM. A paired t test was used for statistical analysis. *p < 0.05, **p < 0.01, ***p < 0.001.

(C) *C. elegans ubql-1(tm1574)* mutants display improved embryonic survival upon IR (40 Gy), compared to N2 WT, indicative of an elevated HRR repair capacity. The *brc-1* mutant strain served as an HRR-defective control. *brc-1(tm1145)* embryos showed increased lethality after IR. The data represent 3 replicate experiments. Error bars represent SD of the mean. A paired t test was used for statistical analysis. *p < 0.05.

(D–F) RPA70- (D), RAD51- (E), and 53BP1 nuclear foci (F) were quantified according to cell-cycle stage. Experiments were analyzed with R, using ordinary two-way ANOVA. Bonferroni post hoc analysis was applied to determine p values of selected pairs defined in a contrast matrix using the R library multcomp. Error bars represent the SD of the mean of 3 replicate wells analyzed in one experiment. Each experiment was carried out twice. Two-way ANOVA with Bonferroni post hoc test, *p < 0.05.

(G) Representative images of MRE11- and ubiquitin (Ub) nuclear foci, using quantitative HCS microscopy for untreated and NCS-treated (500 ng/mL) DMFs. DAPI served as a counterstain. Overlay images were generated between MRE11 and Ub stainings for indicated genotypes. Scale bar, 10 μm.

(H and I) Cells of the indicated genotypes were treated with NCS (500 ng/mL) and stained for nuclear MRE11- (H) and ubiquitin (Ub) foci (I) at the indicated time points. 2,500 cells/well were counted at each time point, and Ub fluorescence was quantified, as in (D)–(F). n = 3 replicate experiments with 2 replicate wells each, mean ± SEM, two-way ANOVA with Bonferroni post hoc test, *p < 0.05.

(J) The overlap area (in %) of MRE11 and Ub foci was calculated by overlay of nuclear foci data generated in (H) and (I) for the indicated genotypes. n = 3 replicate experiments with 2 replicate wells each, mean ± SEM, two-way ANOVA with Bonferroni post hoc test, *p < 0.05.

(K) *ubql-1(tm1574)* mutants display elevated levels of ubiquitinated proteins in the distal germline upon IR, as shown by increased numbers of FK2 stained foci. Scale bar, 10 μm.

(L) For quantification of (K), five germlines per genotype and condition were scored. Error bars represent SD of the mean. A paired t test was used for statistical analysis. *p < 0.05.

See also Figure S5.

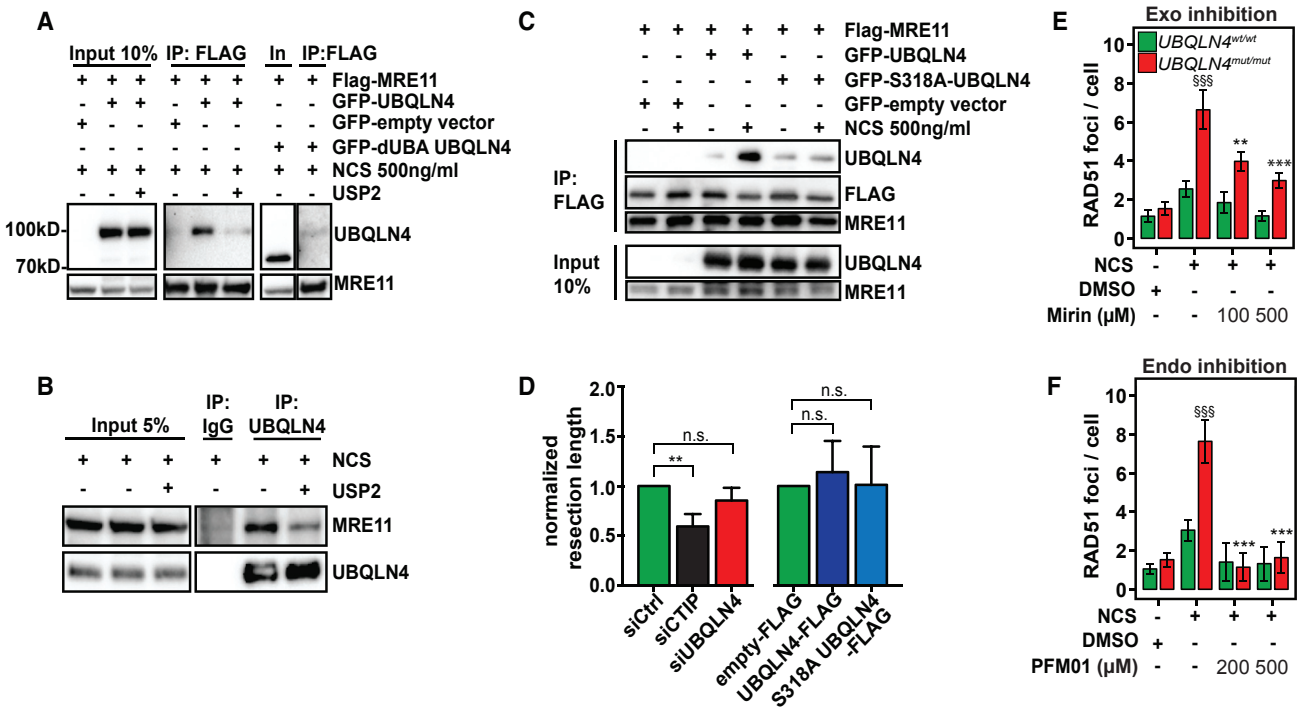

Figure 5. MRE11 Inhibition Represses the Non-physiological HRR in UBQLN4 Mutant Cells

(A) Immunoblot of various GFP-tagged UBQLN4 proteins that co-precipitated with FLAG.MRE11. Immune complexes were obtained from lysates of 293FT cells mock-treated or treated with NCS (500 ng/mL, 1 hr). USP2 (50 nM) was added to the precipitates (30 min at 37°C).

(B) Immunoblot of endogenous UBQLN4 immunoprecipitation or respective IgG control in 293FT cells treated with NCS (500 ng/mL, 1 hr). USP2 (50 nM) was added as in (A).

(C) Immunoblot of various GFP-tagged UBQLN4 proteins that co-precipitated with FLAG.MRE11. Immune complexes were obtained from lysates of 293FT cells mock-treated or treated with NCS (500 ng/mL, 1 hr).

(D) SMART analysis of U2OS cell expressing the indicated constructs. The length of individual fibers was measured and the median of at least 250 fibers was calculated. The average of the medians and the SD of 5 independent experiments are shown. Significance was determined with the paired Student's t test. *$p < 0.05$, **$p < 0.01$.

(E and F) Cells of the indicated genotypes were pre-treated with Mirin (100 or 500 μM) (E), PFM01 (200 or 500 μM) (F), or DMSO 1 hr prior to NCS (500 ng/mL, 10 hr) treatment and stained for nuclear foci of RAD51. 2,000 cells/well were counted, and RAD51 foci were quantified. n = 5, mean ± SEM, two-way ANOVA with Bonferroni post hoc test. §Significance levels between the same cells ± NCS; *significance levels between the same cells in the presence of NCS and ± inhibitor. *$p < 0.05$, **$p < 0.01$, ***$p < 0.001$.

See also Figure S5.

To assess whether MRE11 was ubiquitylated after NCS treatment, we expressed HIS.Ubiquitin and either FLAG.MRE11 or empty vector in HEK293FT cells. Anti-HIS immunoprecipitation revealed NCS-induced co-precipitation of FLAG.MRE11, suggesting that MRE11 was ubiquitylated following DNA damage (Figure S5J). To ask whether UBQLN4 interacted with MRE11 in a ubiquitylation-dependent fashion, we co-expressed FLAG.MRE11 and GFP.UBQLN4 and immunoprecipitated GFP after NCS exposure. FLAG.MRE11 efficiently co-precipitated with GFP.UBQLN4, but not with a GFP control (Figure S5K). Importantly, the FLAG.MRE11:GFP.UBQLN4 interaction was repressed by pre-treatment of the lysates with the deubiquitylating protease USP2 (Figure S5K).

To address whether the interaction between MRE11 and UBQLN4 was dependent on the C-terminal ubiquitin-interacting UBA in UBQLN4, we co-expressed FLAG.MRE11 and either GFP.UBQLN4 or GFP.UBQLN4 lacking the UBA domain (GFP.UBQLN4$^{\Delta UBA}$) in HEK293FT cells. While GFP.UBQLN4 efficiently co-precipitated with anti-FLAG immunoprecipitates, UBQLN4$^{\Delta UBA}$ could not be detected in these precipitates (Figure 5A). We confirmed these data using endogenous immunoprecipitations from NCS-treated HEK293FT cells (Figure 5B). Intriguingly, while FLAG.MRE11 displayed a robust co-precipitation with GFP.UBQLN4^{wt}, this interaction was massively reduced when we expressed GFP.UBQLN4^{S318A}, indicating that this interaction was dependent on ATM-mediated S318/UBQLN4 phosphorylation (Figure 5C). Together, our data provide evidence for a model in which, following DSB induction, UBQLN4 interacts with MRE11 in a ubiquitylation-dependent manner, in order to remove MRE11 from the site of genotoxic damage. In line with a proteasome-dependent turnover of nuclear MRE11, we find that NCS-treated *UBQLN4* mutant cells display significantly increased nuclear ubiquitin and MRE11 staining, compared to WT (Figures S5L–S5N). Importantly, following proteasome inhibition with MG132 for 48 hr, the levels of nuclear ubiquitin and MRE11 staining were similar in

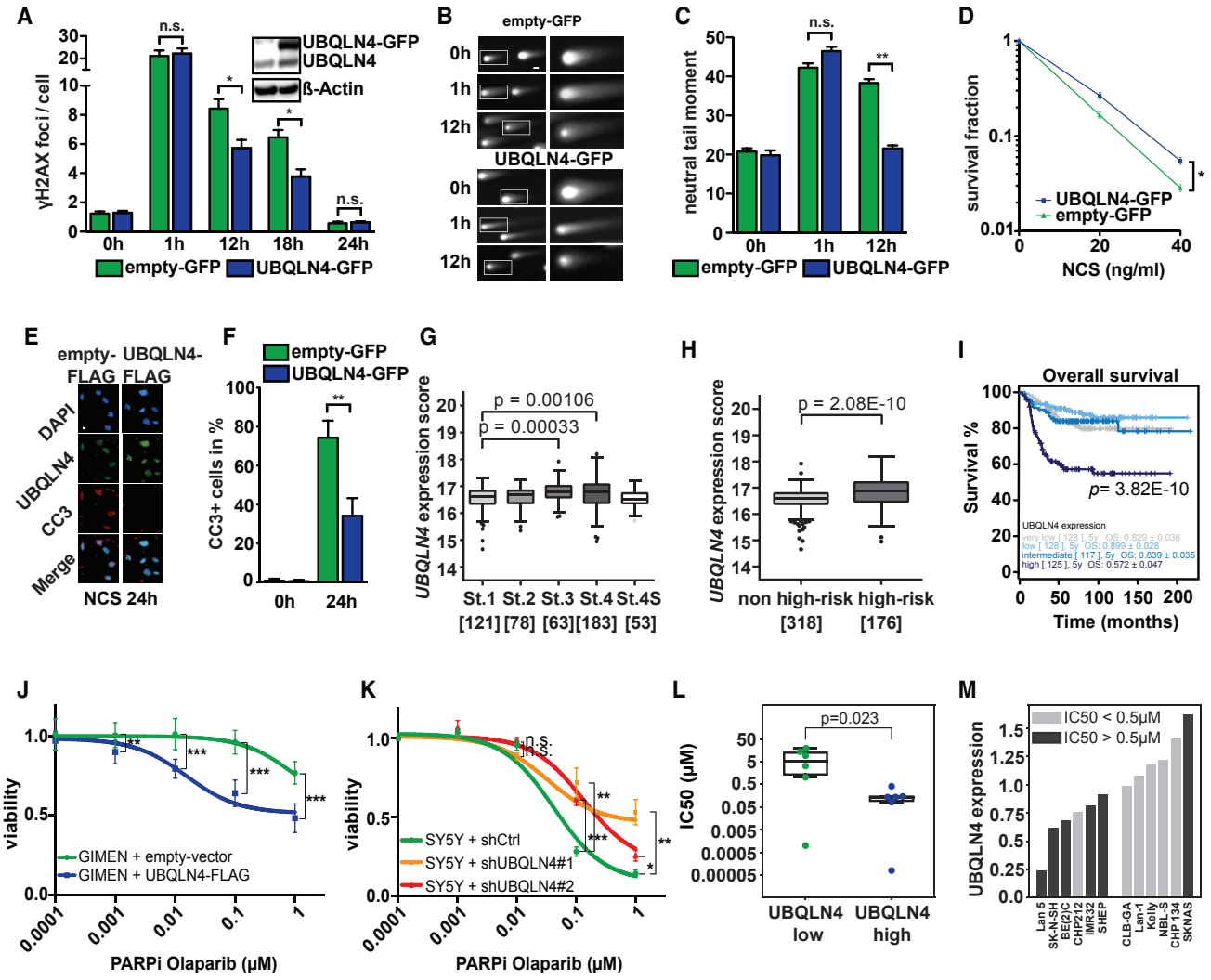

Figure 6. Overexpression of UBQLN4 Is Associated with PARP1 Inhibitor Sensitivity

(A) Number of nuclear γH2AX foci in GFP- or UBQLN4.GFP-expressing U2OS cells after NCS treatment (50 ng/mL) at indicated times. Error bars represent the SD of 1000 cells analyzed in 3 experiments. Statistical significance was determined with paired Student's t test. *p < 0.05. Right-top panel: immunoblot depicting endogenous and ectopic UBQLN4.

(B) Representative images of neutral comet assays of NCS-induced (50 ng/mL) DSBs in GFP- or UBQLN4.GFP-expressing U2OS cells. Scale bar, 10 μm.

(C) Quantification of the data shown in (B). 100 comet tails were assessed per condition. Error bars represent the SD of the mean of the relative comet tail moment analyzed in 3 experiments. Significance was determined with paired Student's t test. *p < 0.05, **p < 0.01.

(D) Clonogenic survival assay of GFP- or UBQLN4.GFP-transduced U2OS cells following NCS exposure. Error bars represent the SD of the mean of n = 3 experiments. p values were calculated using the t test with Welch's correction not assuming equal variance. *p < 0.05.

(E) Immunofluorescence images of FLAG- or UBQLN4.FLAG-transduced U2OS cells treated NCS (500 ng/mL, 24 hr) and stained for UBQLN4 and cleaved-caspase 3 (CC3). Scale bar, 10 μm.

(F) Quantification of CC3-positive cells of the above-mentioned experimental setup. Error bars represent the SD of 1,000 cells analyzed in 3 experiments. Statistical significance was determined with paired Student's t test. *p < 0.05, **p < 0.01.

(G) *UBQLN4* expression levels in 498 neuroblastoma cases classified between stages 1 and 4S according to the International Neuroblastoma Staging System (INSS).

(H) *UBQLN4* expression levels in 498 neuroblastoma cases, classified according to the International Neuroblastoma Risk Group (INRG) staging system into non-high-risk and high-risk neuroblastomas. Samples were reviewed by a pathologist to ensure a minimal tumor content of 60%.

(I) 498 neuroblastoma cases where divided according to *UBQLN4* expression levels into quartiles according to *UBQLN4* expression level: high (n = 125), intermediate (n = 117), low (n = 128), and very low (n = 128) expression. Kaplan-Meier curves show overall survival.

(J) GIMEN cells were stably transfected with empty-vector or FLAG.UBQLN4 and treated with olaparib (96 hr), before intracellular ATP levels were measured, as a surrogate for viability. Error bars represent the SD of the mean of 3 experiments. p values were calculated using the t test with Welch's correction not assuming equal variance. *p < 0.05, **p < 0.01, ***p < 0.001.

(legend continued on next page)

UBQLN4-proficient and -deficient cells (Figures S5M and S5N), suggesting that UBQLN4 controls the proteasome-dependent nuclear MRE11 turnover.

Fitting with a role of MRE11 in initiating DSB end resection, we showed that *UBQLN4* mutant cells, which display aberrant MRE11 retention at sites of DNA damage, show increased numbers of RPA70 and RAD51 nuclear foci, following NCS-induced DNA damage (Figures 4D, 4E, 4G, and 4H). This observation may reflect an increased number of DSBs that are being resected. To verify that the increased number of RPA70 foci in UBQLN4-deficient cells was due to increased resection initiation, rather than enhanced resection processivity, we used the single-molecule analysis of resection track (SMART) resection assay (Cruz-García et al., 2014). This assay reports resection processivity at breaks, in which resection has been initiated, without considering the number of breaks. These experiments revealed that neither UBQLN4 depletion, nor overexpression of FLAG.UBQLN4 or FLAG.UBQLN4^{S318} affect resection processivity (Figure 5D). Our results thus indicate that UBQLN4 depletion leads to increased MRE11-dependent initiation of end-resection and subsequent shifting of more DSBs toward HRR.

To verify MRE11 as a functionally relevant UBQLN4 substrate, we next asked whether MRE11 inhibition with exo- (Mirin) and endonuclease (PFM01) inhibitors overcomes the relatively increased HRR activity in UBQLN4-defective cells. Pre-treatment with Mirin and PFM01 led to a significant inhibition of NCS-induced nuclear RAD51 foci in WT and *UBQLN4* mutant cells (Figures 5E and 5F). In conclusion, our mechanistic data indicate that MRE11 serves a checkpoint function in licensing the HRR process, which is tightly controlled by UBQLN4.

UBQLN4 Overexpression Protects from Genotoxic Stress

Given that *UBQLN4* overexpression results in a relative increase of NHEJ over HRR (Figure 4A) and an absolute decrease of HRR (Figure 4B), we asked whether overall DSB repair capacity may be affected in cells overexpressing UBQLN4. To this end, we assessed DNA repair capacity through immunofluorescence detection of NCS-induced γH2AX foci in U2OS expressing GFP or GFP.UBQLN4. UBQLN4 overexpression resulted in significantly faster clearance of γH2AX foci, starting 12 hr after the initial insult (Figure 6A). Moreover, neutral comet assays demonstrated that cells expressing UBQLN4.GFP sealed NCS-induced DSBs significantly more efficiently than control cells (Figures 6B and 6C). This effect was particularly obvious 12 hr after NCS application. Furthermore, clonogenic survival assays revealed that UBQLN4 overexpression protected cells from the cytotoxic effect of NCS (Figure 6D). Lastly, UBQLN4-overexpressing cells displayed significantly less CC3 positivity (marker of apoptosis) 24 hr after exposure to high-dose NCS, compared to controls (Figures 6E and 6F).

High-Level *UBQLN4* Expression Is Associated with an Actionable PARP1 Inhibitor Sensitivity

To assess the relevance of *UBQLN4* expression in human cancer, we examined 498 neuroblastoma cases (Zhang et al., 2015). *UBQLN4* mRNA expression was significantly increased in stage 3 and 4 neuroblastomas, compared to stage 1 disease (Figure 6G). We further found that *UBQLN4* mRNA levels were significantly increased in high-risk cases (n = 176), compared to non-high-risk patients (n = 318) (Figure 6H). Moreover, high-level *UBQLN4* expression (quartile of patients with high *UBQLN4* expression, n = 125) was associated with reduced event-free survival (EFS) and overall survival (OS), compared to patients displaying intermediate, low or very low *UBQLN4* expression (n = 117, n = 128, n = 128, respectively) (Figures S6A and 6I).

We next assessed *UBQLN4* mRNA levels in breast (n = 5,143), lung (n = 2,437), and ovarian cancer (n = 1,816), using publicly available data (Szász et al., 2016). Again, high *UBQLN4* expression was significantly correlated with reduced OS in these cohorts (Figures S6B–S6D). Further study of the TCGA database (Cancer Genome Atlas Network, 2015) revealed that high *UBQLN4* expression in melanoma (mRNA *Z* score ≥ 2) also results in inferior disease-free survival (DFS) and OS, compared to patients with normal *UBQLN4* expression (mRNA *Z* score <2 and >-2) (Figures S6E and S6F). Moreover, in metastatic melanoma, high *UBQLN4* expression correlated with reduced DFS and OS, compared to patients with low *UBQLN4* expression (Figures S6G and S6H). We further performed immunohistochemistry on melanoma specimens, which were derived from nevus (n = 5), primary melanoma (PRM; n = 8), lymph node metastasized (LNM; n = 10), and distant organ metastasized (DOM; n = 10) samples. UBQLN4 levels were higher in metastasized (DOM, LNM) than in nevus samples (Figures S6I–S6J). Thus, our data derived from distinct entities indicate that high-level *UBQLN4* expression is enriched in high-risk and/or advanced tumors and is associated with reduced OS.

Given that HRR deficiency is associated with sensitivity to PARP1 inhibitors (Dietlein et al., 2014), we profiled olaparib sensitivity in UBQLN4-overexpressing U2OS cells and isogenic controls. UBQLN4 overexpression significantly increased olaparib sensitivity (Figure S6K). We further tested the sensitivity of neuroblastoma cell lines expressing high (SY5Y) or low (GIMEN) UBQLN4 levels and found that SY5Y cells displayed significantly enhanced olaparib sensitivity, compared to GIMEN cells (Figures S6L and S6M). To substantiate the role of UBQLN4 in mediating

(K) SY5Y cells were transduced with control shRNA or 2 shRNAs against *UBQLN4* and treated with olaparib (96 hr). Viability was assessed by CellTiterGlo assays. Error bars represent the SD of the mean of 3 experiments. p values were calculated using the t test with Welch's correction not assuming equal variance. $^{*}p < 0.05$, $^{**}p < 0.01$, $^{***}p < 0.001$.

(L) Neuroblastoma cell lines were treated with olaparib (96 hr) and and viability was assessed by CellTiterGlo assays. IC_{50} values were determined in 3 experiments. Cells were grouped in UBQLN4 low (expression below median) or UBQLN4 high (expression above median). p value was calculated using the Mann-Whitney U test.

(M) Bar chart of the cells reported in (L). Cells are sorted according to their relative UBQLN4 expression. In light gray are cells with IC_{50} below the median, and in dark gray are cells with IC_{50} above the median.

See also Figure S6.

olaparib sensitivity, we depleted *UBQLN4* in SY5Y cells and overexpressed UBQLN4 in GIMEN cells (Figures S6N and S6O). As shown in Figures 6J and 6K, UBQLN4 overexpression in GIMEN cells significantly increased olaparib sensitivity, whereas UBQLN4 depletion in SY5Y cells significantly increased their olaparib resistance. Of note, neither SY5Y nor GIMEN cells are *MYCN* amplified. To test whether high-level UBQLN4 retains its predictive value in *MYCN*-amplified cells, we examined olaparib sensitivity in NMB and SKNDZ neuroblastoma cell lines, which display high- and low-level UBQLN4 expression, respectively (Harenza et al., 2017) (Figure S6P). Increased olaparib sensitivity was preserved in NMB cells, whereas SKNDZ cells were more resistant (Figure S6Q). We next assessed the olaparib response in a panel of 12 additional neuroblastoma cell lines and found that cells expressing high UBQLN4 levels showed a significantly increased olaparib sensitivity, compared to cells with low expression (Figures 6L and 6M). These data indicate that elevated UBQLN4 levels are associated with PARP1 inhibitor sensitivity.

DISCUSSION

The UBQLN4 deficiency syndrome described here is characterized by clinical symptoms frequently detected in genome instability syndromes (Hoeijmakers, 2001). Here, we demonstrated that UBQLN4 deficiency led to marked cellular sensitivity to genotoxic stress, that UBQLN4 was recruited to sites of DNA damage, and that it was an ATM substrate in the DDR. Importantly, the ATM-mediated phosphorylation was functionally significant for the role of UBQLN4 in the DDR.

Mechanistically, we showed that UBQLN4 impacted on DSB repair pathway choice. It has recently become evident that maintenance of the exquisite balance between these pathways is critical for timely DSB repair and genome maintenance (Baranes-Bachar et al., 2018). We found that the NHEJ:HRR ratio in UBQLN4-depleted cells was skewed toward HRR, while ectopic UBQLN4 overexpression resulted in a relative increase in NHEJ-driven DSB sealing over HRR. These observations were further confirmed in *C. elegans,* where *ubql-1* mutants displayed increased HRR proficiency. Importantly, *UBQLN4* overexpression resulted in an absolute decrease in HRR usage. Further mechanistic insight into these effects came from the observation that the apical HRR regulator MRE11 was retained at sites of DSBs in UBQLN4-deficient cells. We further revealed that MRE11 was ubiquitylated following DNA damage and demonstrated that UBQLN4 specifically interacted with ubiquitylated MRE11 in response to DNA damage. Moreover, this interaction depended on the UBA domain of UBQLN4, as well as ATM-mediated S318/UBQLN4 phosphorylation. Finally, we showed that excessive RAD51 foci formation following NCS treatment in UBQLN4-deficient cells could be reverted to normal levels, when the endo- or exonuclease activities of MRE11 were pharmacologically inhibited. Based on our data, it is tempting to speculate that a potential function of UBQLN4 within the DDR is to assist in the timely removal of DDR factors, such as MRE11, from damaged chromatin, in order to prevent inappropriate DSB end resection and subsequent HRR. However, we note that our data do not exclude the possibility that UBQLN4 has additional interaction partners within and outside of the DDR. A dose-dependent role for UBQLN4 in promoting the use of NHEJ is supported by the DSB repair reporter assays. The relative increase in NHEJ usage in *UBQLN4*-overexpressing cells may be driven by the functional repression of HRR through the removal of HRR factors, such as MRE11, from damaged chromatin. Thus, when the UBQLN4 level is altered in either direction, the NHEJ:HRR ratio is markedly affected.

Our data suggest a primarily nuclear role of UBQLN4. However, UBQLN4 does not contain an obvious nuclear localization sequence. In line with this, we also find a fraction of UBQLN4 localized in the cytoplasm (Figures S3N and S4J). Moreover, UBQLN1, which shares ~71% amino acid sequence homology with UBQLN4, is involved in triaging incorrectly targeted membrane proteins in the cytosol to a ubiquitin ligase to promote degradation (Itakura et al., 2016). Thus, it is conceivable that UBQLN4 is relocated to the nucleus following decoration with a yet unidentified post-translational modification.

We found a correlation between poor OS and elevated *UBQLN4* expression in neuroblastoma, melanoma, and ovarian, breast, and lung cancer. Our data indicate that *UBQLN4* overexpression may be a selected event in different cancer entities. We provide a rationale for this observation by showing that *UBQLN4* overexpression in cultured cells enhances DSB sealing, reduces apoptosis, and increases survival, following NCS treatment. It is conceivable that *UBQLN4* overexpression is selected in cancer cells, since it facilitates effective coping with endogenous DSBs, such as those occurring during replicative stress. While this largely NHEJ-mediated, more effective DSB sealing in *UBQLN4*-overexpressing cells protects them from acute genotoxic stress, it is likely to be highly mutagenic, as NHEJ is an error-prone mechanism (Dietlein et al., 2014). Thus, NHEJ-driven mutagenesis may also be selected for in cancer cells, since it further promotes genome instability and oncogenic transformation.

Defective HRR in the context of *BRCA1* or *BRCA2* loss-of-function mutations is associated with PARP1 inhibitor sensitivity (Dietlein et al., 2014). Consistent with an HRR defect in *UBQLN4*-overexpressing cells, we found that cells with high UBQLN4 expression were significantly more sensitive to olaparib than cells with low *UBQLN4* expression. It was recently proposed that NHEJ promotes genomic instability and cytotoxicity in HRR-deficient cells treated with PARP1 inhibitors (Patel et al., 2011). In extrapolation of these data, the enhanced NHEJ observed in *UBQLN4*-overexpressing cells may contribute to the toxicity inflicted by PARP1 inhibitors in these cells.

Altogether, our data reveal the biology of a new genome instability syndrome, provide evidence of a role for UBQLN4 in regulating DSB repair pathway choice, and identify *UBQLN4* overexpression as a predictor of poor survival in various cancer entities that is associated with an actionable sensitivity to PARP1 inhibitors.

STAR★METHODS

Detailed methods are provided in the online version of this paper and include the following:

- KEY RESOURCES TABLE
- CONTACT FOR REAGENT AND RESOURCE SHARING

SUPPLEMENTAL INFORMATION

Supplemental Information includes six figures and three tables and can be found with this article online at https://doi.org/10.1016/j.cell.2018.11.024.

ACKNOWLEDGMENTS

We are grateful to our patients and their families. We thank M. Cemel-David and E. Tal for experimental guidance and A. Klartag, D. Falkenstein, and A. Krebs-Roszyk for technical assistance. We thank Dr. T. Kurz for sharing unpublished information. Some analyses conducted here were based on data that was generated by The Cancer Genome Atlas. This work was funded through the Dr. M. and S.G. Adelson Medical Research Foundation, The Israel Science Foundation joint ISF-NSFC Research Program and The Israel Cancer Research Fund (to Y.S.), the German-Israeli Foundation for Research and Development (I-65-412.20-2016 to Y.S. and H.C.R.), the Deutsche Forschungsgemeinschaft (KFO-286-RP2 to H.C.R., KFO-286-CP2 to M.P., JA2439/1-1 to R.D.J., DI1731/2-1 to F.D.), the Else Kröner-Fresenius Stiftung (2014-A06 to H.C.R., 2016_Kolleg.19 to R.D.J.), the Deutsche Krebshilfe (1117240 to H.C.R. and the Mildred-Scheel Professorship to M.P.), the German Ministry of Education and Research (BMBF 01GM1211B to D.W., BMBF e:Med 01ZX1303A and 01ZX1406 to M.P., BMBF e:Med 01ZX1303 and 01ZX1307 to M.F.), and R+D+I grants from the Spanish Ministry of Economy and Competitivity (SAF2013-43255-P and SAF2016-74855-P to P.H.). Y.S. is a Research Professor of the Israel Cancer Research Fund.

AUTHOR CONTRIBUTIONS

Conceptualization, R.D.J., Y.Z., D.W., H.C.R., and Y.S.; Methodology, R.D.J., Y.Z., H.C.R., D.W., and Y.S.; Investigation, R.D.J., F.B., J.I., B.B.V., J.G., M.A.B., A.S., C.C-R., M.A.D., K.B.-B., C.B., A.S., J.L.W., F.H., N.T., T.N., H.-J.L., M.K., T.G., D.S.B.H., P.H., M.P., T.H., and M.F.; Patient Enrollment, F.B., F.D., H.-J.L., B.A., and D.W.; Writing, R.D.J., H.C.R., D.W., and Y.S.; Visualization, R.D.J., F.B., and J.I.; Funding Acquisition, R.D.J., M.P., P.H., H.C.R., D.W., and Y.S.; Supervision, H.C.R. and Y.S.

DECLARATION OF INTERESTS

H.C.R. received consulting fees from Abbvie, AstraZeneca, Vertex, and Merck and research funding from Gilead.

Received: December 1, 2017
Revised: August 31, 2018
Accepted: November 16, 2018
Published: January 3, 2019

REFERENCES

Baranes-Bachar, K., Levy-Barda, A., Oehler, J., Reid, D.A., Soria-Bretones, I., Voss, T.C., Chung, D., Park, Y., Liu, C., Yoon, J.B., Li, W., Dellaire, G., Misteli, T., Huertas, P., Rothenberg, E., Ramadan, K., Ziv, Y., and Shiloh, Y. (2018). The ubiquitin E3/E4 ligase UBE4A adjusts protein ubiquitylation and accumulation at sites of DNA damage, facilitating double-strand break repair. Mol. Cell *69*, 866–878.

Cancer Genome Atlas Network (2015). Genomic classification of cutaneous melanoma. Cell *161*, 1681–1696.

Cox, J., Neuhauser, N., Michalski, A., Scheltema, R.A., Olsen, J.V., and Mann, M. (2011). Andromeda: A peptide search engine integrated into the MaxQuant environment. J. Proteome Res. *10*, 1794–1805.

Cruz-García, A., López-Saavedra, A., and Huertas, P. (2014). BRCA1 accelerates CtIP-mediated DNA-end resection. Cell Rep. *9*, 451–459.

Dietlein, F., Thelen, L., and Reinhardt, H.C. (2014). Cancer-specific defects in DNA repair pathways as targets for personalized therapeutic approaches. Trends Genet. *30*, 326–339.

Dull, T., Zufferey, R., Kelly, M., Mandel, R.J., Nguyen, M., Trono, D., and Naldini, L. (1998). A third-generation lentivirus vector with a conditional packaging system. J. Virol. *72*, 8463–8471.

Grice, G.L., and Nathan, J.A. (2016). The recognition of ubiquitinated proteins by the proteasome. Cell. Mol. Life Sci. *73*, 3497–3506.

Harding, S.M., and Greenberg, R.A. (2016). Choreographing the double strand break response: Ubiquitin and SUMO control of nuclear architecture. Front. Genet. *7*, 103.

Harenza, J.L., Diamond, M.A., Adams, R.N., Song, M.M., Davidson, H.L., Hart, L.S., Dent, M.H., Fortina, P., Reynolds, C.P., and Maris, J.M. (2017). Transcriptomic profiling of 39 commonly-used neuroblastoma cell lines. Sci. Data *4*, 170033.

Hartmann-Petersen, R., Seeger, M., and Gordon, C. (2003). Transferring substrates to the 26S proteasome. Trends Biochem. Sci. *28*, 26–31.

Hoeijmakers, J.H. (2001). Genome maintenance mechanisms for preventing cancer. Nature *411*, 366–374.

Hu, Y., Park, K.K., Yang, L., Wei, X., Yang, Q., Cho, K.S., Thielen, P., Lee, A.H., Cartoni, R., Glimcher, L.H., et al. (2012). Differential effects of unfolded protein response pathways on axon injury-induced death of retinal ganglion cells. Neuron *73*, 445–452.

Itakura, E., Zavodszky, E., Shao, S., Wohlever, M.L., Keenan, R.J., and Hegde, R.S. (2016). Ubiquilins chaperone and triage mitochondrial membrane proteins for degradation. Mol. Cell *63*, 21–33.

Kaplun, L., Tzirkin, R., Bakhrat, A., Shabek, N., Ivantsiv, Y., and Raveh, D. (2005). The DNA damage-inducible UbL-UbA protein Ddi1 participates in Mec1-mediated degradation of Ho endonuclease. Mol. Cell. Biol. *25*, 5355–5362.

Ko, H.S., Uehara, T., Tsuruma, K., and Nomura, Y. (2004). Ubiquilin interacts with ubiquitylated proteins and proteasome through its ubiquitin-associated and ubiquitin-like domains. FEBS Lett. *566*, 110–114.

Lemmens, B.B., and Tijsterman, M. (2011). DNA double-strand break repair in Caenorhabditis elegans. Chromosoma *120*, 1–21.

Levy-Barda, A., Lerenthal, Y., Davis, A.J., Chung, Y.M., Essers, J., Shao, Z., van Vliet, N., Chen, D.J., Hu, M.C., Kanaar, R., et al. (2011). Involvement of the nuclear proteasome activator PA28γ in the cellular response to DNA double-strand breaks. Cell Cycle *10*, 4300–4310.

López-Saavedra, A., Gómez-Cabello, D., Domínguez-Sánchez, M.S., Mejías-Navarro, F., Fernández-Ávila, M.J., Dinant, C., Martínez-Macías, M.I., Bartek, J., and Huertas, P. (2016). A genome-wide screening uncovers the role of CCAR2 as an antagonist of DNA end resection. Nat. Commun. *7*, 12364.

Matsuoka, S., Ballif, B.A., Smogorzewska, A., McDonald, E.R., 3rd, Hurov, K.E., Luo, J., Bakalarski, C.E., Zhao, Z., Solimini, N., Lerenthal, Y., et al. (2007). ATM and ATR substrate analysis reveals extensive protein networks responsive to DNA damage. Science *316*, 1160–1166.

Ng, J.M., Vermeulen, W., van der Horst, G.T., Bergink, S., Sugasawa, K., Vrieling, H., and Hoeijmakers, J.H. (2003). A novel regulation mechanism of DNA repair by damage-induced and RAD23-dependent stabilization of xeroderma pigmentosum group C protein. Genes Dev. *17*, 1630–1645.

Olive, P.L., and Banáth, J.P. (2006). The comet assay: A method to measure DNA damage in individual cells. Nat. Protoc. *1*, 23–29.

Patel, A.G., Sarkaria, J.N., and Kaufmann, S.H. (2011). Nonhomologous end joining drives poly(ADP-ribose) polymerase (PARP) inhibitor lethality in homologous recombination-deficient cells. Proc. Natl. Acad. Sci. USA *108*, 3406–3411.

Reinhardt, H.C., and Yaffe, M.B. (2013). Phospho-Ser/Thr-binding domains: Navigating the cell cycle and DNA damage response. Nat. Rev. Mol. Cell Biol. *14*, 563–580.

Shiloh, Y., and Ziv, Y. (2013). The ATM protein kinase: Regulating the cellular response to genotoxic stress, and more. Nat. Rev. Mol. Cell Biol. *14*, 197–210.

Stewart, S.A., Dykxhoorn, D.M., Palliser, D., Mizuno, H., Yu, E.Y., An, D.S., Sabatini, D.M., Chen, I.S., Hahn, W.C., Sharp, P.A., et al. (2003). Lentivirus-delivered stable gene silencing by RNAi in primary cells. RNA *9*, 493–501.

Symington, L.S., and Gautier, J. (2011). Double-strand break end resection and repair pathway choice. Annu. Rev. Genet. *45*, 247–271.

Szász, A.M., Lánczky, A., Nagy, Á., Förster, S., Hark, K., Green, J.E., Boussioutas, A., Busuttil, R., Szabó, A., and Győrffy, B. (2016). Cross-validation of survival associated biomarkers in gastric cancer using transcriptomic data of 1,065 patients. Oncotarget *7*, 49322–49333.

Walczak, H., Iwai, K., and Dikic, I. (2012). Generation and physiological roles of linear ubiquitin chains. BMC Biol. *10*, 23.

Zhang, W., Yu, Y., Hertwig, F., Thierry-Mieg, J., Zhang, W., Thierry-Mieg, D., Wang, J., Furlanello, C., Devanarayan, V., Cheng, J., et al. (2015). Comparison of RNA-seq and microarray-based models for clinical endpoint prediction. Genome Biol. *16*, 133.

STAR★METHODS

KEY RESOURCES TABLE

REAGENT or RESOURCE	SOURCE	IDENTIFIER
Antibodies		
Mouse anti-UBQLN4, clone A333	Santa Cruz Biotechnology	Cat#: sc-136145; RRID: AB_2009286
Rabbit anti-UBQLN4	Lifespan Biosciences	Cat#: LS-C108556; RRID:AB_10635383
Rabbit anti-UBQLN4	Bethyl	Cat#: A300-BL20642; RRID: N/A
Rabbit anti-phospho-UBQLN4(S318)	Bethyl	Cat#: A300-BL20645; RRID: N/A
Mouse anti-phospho-Histone H2A.X (Ser139), clone JBW301	Millipore	Cat#: 05-636; RRID: AB_309864
Rabbit anti-RAD51	Millipore	Cat#: PC130; RRID: AB_2238184
Mouse α-Tubulin, clone TUB-1A2	Abcam	Cat#: ab11325; RRID: AB_2210526
Mouse anti-53BP1	Millipore	Cat#: MAB3802; RRID: AB_11212586
Mouse anti-ubiquitinylated proteins, clone FK2	Millipore	Cat#: 04-263; RRID: AB_612093
Mouse anti-Flag	Santa Cruz Biotechnology	Cat#: sc-166355; RRID: AB_2017593
Mouse anti-HSP90, clone 68	BD Biosciences	Cat#: 610418; RRID: AB_397798
Mouse β-Actin, clone AC-74	Sigma-Aldrich	Cat#: A5316; RRID: AB_476743
Rabbit anti-phospho-KAP1(S824)	Bethyl	Cat#: A300-767A; RRID: AB_669740
Rabbit anti-MRE11	Novus	Cat#: NB 100-142; RRID: AB_350079
Rabbit anti-Histone H3	Abcam	Cat#: ab1791; RRID: AB_302613
Mouse anti-His	GenScript	Cat#: A00186, RRID: AB_914704
Mouse IgG	Santa Cruz Biotechnology	Cat#: sc-2025; RRID: AB_737182
Rabbit anti-Caspase 3, Active Form	BD Biosciences	Cat#: 559565; RRID: AB_397274
Anti-BrdU	GE Healthcare	Cat#: RPN202; RRID: AB_2314032
Goat Alexa Fluor 488 anti-mouse	Invitrogen	Cat#: A-11001; RRID: AB_2534069
Goat Alexa Fluor 647 anti-mouse	Invitrogen	Cat#: A-21235; RRID: AB_2535804
Goat Alexa Fluor 488 anti-rabbit	Invitrogen	Cat#: A-11008; RRID: AB_143165
Goat Alexa Fluor 647 anti-rabbit	Invitrogen	Cat#: A27040; RRID: AB_2536101
Goat anti-rabbit IgG peroxidase	EMD Millipore	Cat#: AP132P; RRID: AB_90264
Goat anti-mouse IgG peroxidase	EMD Millipore	Cat#: 12-349; RRID: AB_390192
Bacterial and Virus Strains		
E. coli stable competent (high efficiency)	New England Biolabs	Cat#: C3040I
Chemicals, Peptides, and Recombinant Proteins		
Neocarzinostatin	Sigma-Aldrich	Cat#: N9162
DNA-PK Inhibitor KU60648	Selleck Chemicals	Cat#: S8045
ATM Inhibitor KU60019	Selleck Chemicals	Cat#: S1570
Etoposide	Hexal	N/A
Cisplatin	Accord	N/A
Hydroxyurea	Sigma-Aldrich	Cat#: H8627
Camptothecin	Millipore	Cat#: 208925
USP2	BostonBiochem	Cat#: E-504
ATR Inhibitor AZ20	Selleck Chemicals	Cat#: S7050
Mirin	Sigma-Aldrich	Cat#: M9948
PFM01	Sigma-Aldrich	Cat#: SML1735
PARP1 Inhibitor olaparib	MedChem Express	Cat#: HY-10162/CS-0075
MG132	Selleck Chemicals	Cat#: S2619
ProLong® Gold Antifade Reagent	Molecular Probes	Cat#: P-36931

(*Continued on next page*)

Continued

REAGENT or RESOURCE	SOURCE	IDENTIFIER
CellTiter-Glo® Reagent	Promega	Cat#: G7573
N-Ethylmaleimide (NEM)	Sigma-Aldrich	Cat#: E3876
Puromycin	Sigma-Aldrich	Cat#: P8833
G418	Sigma-Aldrich	Cat#: G418-RO
Polybrene	Sigma Aldrich	H9268-10G
LysC	Wako	Cat#: 125-05061
GluC	Promega	Cat#: V1651
Trypsin	Promega	V5113
Dharmafect-1	Dharmacon	T-2001-01
Critical Commercial Assays		
Subcellular Protein Fractionation Kit	Thermo Fisher	78840
TruSeq Sample Preparation Kit v2	Illumina	FC-121-2001
TiO2 Phosphopeptide Enrichment Kit	Thermo Fisher	A32993
SeqCap EZ Exome v3.0 Kit	Roche	06465692001
Agilent DNA 1000 kit	Agilent	5067-1504
QuickChange II Site-Directed Mutagenesis Kit	Agilent	200523
Deposited Data		
Quantative high-content (HCS) microscopy raw and analyzed data	This paper, Mendeley data	https://doi.org/10.17632/gz4xvwbvhs.1
Phospho-proteomic mass-spectrometry raw and analyzed data	This paper, ProteomeXChange Consortium, dataset identifier: PXD011488	https://www.ebi.ac.uk/pride/archive/login Username: reviewer13154@ebi.ac.uk Password: 8Mob4SuW
Experimental Models: Cell Lines		
Human Dermal Fibroblasts Patient A-IV-4	isolated from patient	N/A
Human Dermal Fibroblasts Patient A-IV-5	isolated from patient	N/A
Human Dermal Fibroblasts Patient B-IV-3	isolated from patient	N/A
Human Dermal Fibroblasts Parent B-III-2	isolated from patient	N/A
Human Dermal Fibroblasts WT_1	isolated from patient	N/A
Human Dermal Fibroblasts WT_2	isolated from patient	N/A
U2-OS	ATCC	HTB-96
HEK293FT	ThermoFisher Scientific	R70007
U2-OS-SSR-GFP	Huertas Lab, Sevilla, Spain	N/A
U2-OS-DR-GFP	Huertas Lab, Sevilla, Spain	N/A
MDA-231-MB UBQLN4 CRISPR KO	This paper	N/A
CHP212	Fischer Lab, Cologne, Germany (confirmation DSMZ 2007)	CRL-2273 (ATCC)
Kelly	Fischer Lab, Cologne, Germany (confirmation DSMZ 2007)	ACC 355
BE(2)C	Witt/Deubzer Lab, Essen, Germany	CRL-2268 (ATCC)
Lan5	DSMZ 2013	ACC 673
IMR32	DSMZ 2006	ACC 165
Lan-1	DSMZ 2013	ACC 635
CHP134	DSMZ 2013	ACC 653
SHEP	Fischer Lab, Cologne, Germany	N/A
SK-N-SH	ATCC 2014	HTB-11

(*Continued on next page*)

Continued

REAGENT or RESOURCE	SOURCE	IDENTIFIER
SKNAS	Fischer Lab, Cologne, Germany (confirmation DSMZ 2007)	CRL-2137 (ATCC)
CLB-GA	Schulte Lab, Essen, Germany (confirmation DSMZ 2014)	N/A
NBL-S	DSMZ 2014	ACC 656
SY5Y	Fischer Lab, Cologne, Germany (confirmation DSMZ 2007)	ACC 209 (DSMZ)
GIMEN	DSMZ 2014	ACC 654
SKNDZ	ATCC 2014	CRL-2149
NMB	DSMZ 2013	ACC 657
Experimental Models: Organisms/Strains		
C. elegans: strain N2 Bristol	Caenorhabditis Genetics Center	WB Strain: N2; *C. elegans* wild isolate
C. elegans: strain FX1574: *ubql-1(tm1574)* I.	National BioResource Project (NBRP) SHIGEN Mitani	NBRP Strain: FX1574; WormBase: WBVar00250560; http://shigen.nig.ac.jp/shigen/index.jsp
C. elegans: strain DW102: *brc-1 (tm1145)* III.	Caenorhabditis Genetics Center	WB Strain: DW102; Wormbase: DW102
Oligonucleotides		
siRNA targeting sequence UBQLN4 pool	Dharmacon	Cat#: L-021178-01
siRNA CTIP	Huertas Lab	N/A
siRNA non-targeted (Ctrl)	Huertas Lab	N/A
shRNA (pLKO.1) UBQLN4 #1 CCGGCCAGAGGAAATTCGTGTGAAACTC GAGTTTCACACGAATTTCCTCTGGTTTTT	Sigma-Aldrich	Cat#: SHCLNG-NM_020131; TRCN0000007738
shRNA (pLKO.1) UBQLN4 #2 CCGGGCTGCTCAGATGATGGTGAATCTC GAGATTCACCATCATCTGAGCAGCTTTTT	Sigma-Aldrich	Cat#: SHCLNG-NM_020131; TRCN0000007741
shRNA (pLKO.1) non-targeted (Ctrl)	Sigma-Aldrich	Cat#: SHC016
Recombinant DNA		
UBQLN4 cDNA cloned in pCDNA3.1	Gift from Vivian Su	N/A
GFP.UBQLN4 cloned in plncx2	This paper	N/A
GFP.UBQLN4.S318A in plncx2	This paper	N/A
GFP.UBQLN4.S318D in plncx2	This paper	N/A
GFP.UBQLN4-dUBA in plncx2	This paper	N/A
GFP.UBQLN4-dUBL in plncx2	This paper	N/A
GFP in plncx2	This paper	N/A
3xFLAG.UBQLN4 cloned in pBabe.puro	This paper	N/A
3xFLAG.UBQLN4 in pBabe.puro	This paper	N/A
3xFLAG.UBQLN4-S318A in pBabe.puro	This paper	N/A
3xFLAG in pBabe.puro	Gift from Ron Prywes	N/A
FLAG.MRE11 cloned in pCDNA3.1	This paper	N/A
HIS.Ub cloned in pCDNA3.1	Gift from Aart G. Jochemsen	N/A
pMDLg/pRRE	Dull et al., 1998	Addgene Plasmid #12251
pMD2.G	Dull et al., 1998	Addgene Plasmid #12259
pRSV-Rev	Dull et al., 1998	Addgene Plasmid #12253
pCMV-VSV-G	Stewart et al., 2003	Addgene Plasmid #8454
Software and Algorithms		
ImageJ software with the PZfociEZ plugin	Wayne Rasband (NIH)	https://imagej.nih.gov/ij/
Comet Score software	TriTek	http://rexhoover.com
R v3.4.3	The R Foundation	https://www.r-project.org

(*Continued on next page*)

Continued

REAGENT or RESOURCE	SOURCE	IDENTIFIER
NIS ELEMENTS	Nikon	https://www.nikoninstruments.com/
Adobe Photoshop CS4 (DNA fiber analysis)	Adobe	https://www.adobe.com/
Adobe Illustrator	Adobe	https://www.adobe.com/
MaxQuant v1.5.3.8	Cox et al., 2011	http://www.coxdocs.org/doku.php?id=maxquant:common:download_and_installation#download_and_installation_guide
Cellomics software package (Colocalization V.4 Bioapplication)	Thermo Scientific	https://www.thermofisher.com/de/de/home/life-science/cell-analysis/cellular-imaging/high-content-screening/high-content-screening-instruments/hcs-studio-2.html
PRISM	Graphpad	https://www.graphpad.com
Kaluza	Beckman Coulter	https://www.beckman.com/coulter-flow-cytometers/software/kaluza
Python v3.6.5	Python Software Foundation	https://www.python.org
GATK v3.7	Broad Institute	https://software.broadinstitute.org/gatk
BWA v0.7.15	SourceForge	http://bio-bwa.sourceforge.net
Annovar v2016.02.01	N/A	http://annovar.openbioinformatics.org/en/latest/
Other		
CometAssay system	Trevigen	4250-050-K
Glass Bottom dishes 35mm	MatTek	P35G-0-10-C
FLAG M2 beads	Sigma-Aldrich	M8823
HIS Ni-NTA beads	QIAGEN	36111
GFP-trap beads	Chromotek	gtma-20
MagneTM Protein A Beads	Promega	G878A

CONTACT FOR REAGENT AND RESOURCE SHARING

Further information and requests for resources and reagents should be directed to and will be fulfilled by the Lead Contact, H. Christian Reinhardt (christian.reinhardt@uk-koeln.de). The raw whole-exome sequencing data that support the findings in patients cannot be made publicly available for confidentiality reasons. Qualified researchers may apply for access to the sequencing raw data, pending institutional review board approval.

EXPERIMENTAL MODEL AND SUBJECT DETAILS

Human subjects

Written informed consent was obtained from the UBQLN4 deficiency syndrome families for participation in this study. The study was performed according to the Declaration of Helsinki protocols and was approved by the local institutional review board in Essen (ethics vote 12-5089-BO for CRANIRARE). All subjects were not involved in previous procedures.

Patient A-IV-4 - c.f. Figure 1A, Figures S2A–S2M

Pregnancy was complicated by nuchal edema and polyhydramnios. Birth occurred at 35 weeks of gestation with a weight of 1960 g (- 1.5 SD), a length of 47 cm (−0.3 SD) and occipitofrontal circumference (OFC) of 33 cm (mean). The patient had a respiratory failure that required mechanical ventilation. At birth, he exhibited hypertelorism, microphthalmia, micrognathia, dysplastic and low-set ears with overfolded helices, a right-sided preaxial polydactyly, and bilateral simian creases (Figures S2B–S2F). Re-examination at the age of 5 $^{4}/_{12}$ years revealed low body measurements [weight: 11 kg (−5.5 SD), length: 102 cm (−2.5 SD), OFC: 47.5 cm (−3.4 SD)]. He was able to crawl, but not walk without support. Deafness and a cryptorchidism were noted as well as proptosis, downward slanting palpebral fissures, and dysplastic ears (Figures S2G–S2I). At 11 years of age all body measurements were low [height: 116 cm (−4.1 SD), weight: 16 kg (−10.9 SD) and OFC: 48 cm (−4.8 SD)]. The facial dysmorphisms remained (Figures S2J–S2L) and dry skin and prominent veins were noted, especially on the forehead and chest. A sleep disorder was reported by the mother, as well as abnormal feeding behavior with constant craving for food, notable in view of the low weight gain. No abnormal reaction to sunlight was reported other than light-sensitive eyes. Blood count showed anemia with a hemoglobin of

10.5 g/dl (reference: 11.8-14.9 g/dl), MCV of 76.0 fl (reference: 77-95 fl), MCHC of 30.7 g Hb/dl (reference: 31-39 g Hb/dl). Neurological examination revealed spasticity of the lower extremities with brisk reflexes and contractures of both knees. The patient was able to walk independently, presenting insecure circumduction gait pattern. The upper extremities showed slightly increased muscle tone with almost normal function of small hand muscles. Muscle tone of the trunk was reduced. Cranial nerve examination revealed no anomalies apart from esotropia and saccadic eye movements. Speech development was markedly retarded, but he was still able to produce double syllables. The patient presented stereotypic autistic gestures such as body rocking and head nodding, and self-biting and pinching was reported by the mother. Exome sequencing revealed the homozygous mutation chr1:g.156,044,148G > A [GRCh38/hg38]; c.976C > T (GenBank: NM_020131.4); p.(Arg326Ter) (NP_064516.2) in the *UBQLN4* gene.

Patient B-IV-3 - c.f. Figure 1B, Figures S2N–S2W

Pregnancy was complicated by nuchal edema and oligohydramnios. Birth occurred at 38 weeks of gestation with: [weight: 1970 g (- 3.0 SD), length: 46 cm (−2.2 SD) and OFC: 33.5 cm (- 1.0 SD)]. At 7 weeks of age, proptosis, large nose, small mouth and micrognathia were noted. At the age of $1\,^{3}/_{12}$ years low anthropometric measures were observed: [weight: 7500 g (−2.8 SD), length: 75 cm (−1.8 SD), OFC: 46 cm (−1.7 SD)]. The patient was unable to crawl or sit and did not speak. Deafness was diagnosed as well as hypotelorism, brachycephaly, cryptorchidism, hypoplastic nails, and abnormal semicircular canals. At the age of $6\,^{1}/_{12}$ years anthropometric measures were low: [height: 100 cm (−3.8 SD), weight: 15 kg (−3.2 SD) and OFC: 50 cm (−1.7 SD)], and the patient was unable to walk or speak. Proptosis, large nose, short philtrum, camptodactyly of fingers IV/V, contractures of both knees and cryptorchidism were observed (Figures S2P–S2R). Recurrent respiratory tract infections reported. At the age of $10\,^{2}/_{12}$ years, body measurements were: [height: 117 cm (−3.7 SD), weight: 16.9 kg (−5.6 SD) and OFC: 50.5 cm (−2.4 SD)]. Facial dysmorphisms did not change, and hirsutism, prominent scalp veins, dry skin and three very dark nevi on the soles were observed (Figures S2S–S2W). Sleep disturbances were reported as well as abnormal feeding behavior with constant craving for food. There was no abnormal reaction to sunlight. Microcytic-hypochromic anemia was identified. Neurological examination revealed spasticity of the lower extremities with contractures of the knees. The patient was unable to walk independently. The upper extremities showed slightly increased muscle tone with almost normal function of small hand muscles, and reduced muscle tone of the trunk. Cranial nerve examination revealed difficulties initiating pursuit eye movements but the nerve was otherwise normal. There was no progress in speech development. Stereotypic autistic behavior (repetitive noise making, teeth grinding) was observed. Exome sequencing revealed the homozygous mutation chr1:g.156,044,148G > A [GRCh38/hg38]; c.976C > T (GenBank: NM_020131.4); p.(Arg326Ter) (NP_064516.2) in the *UBQLN4* gene.

Patients A-IV-3 and A-IV-5 -c.f. Figure 1A

Further clinical information regarding patient A-IV-3 and A-IV-5 can be found in Table S1.

C. elegans strains and maintenance

All worms (age: day 1 of adulthood; sex: hermaphrodites) were grown and maintained at 20°C on nematode growth medium (NGM) agar plates seeded with the *E. coli* strain OP50 as food source. The Bristol strain N2 was used as wt. Strain DW102 *brc-1(tm1145)* served as positive control for the HRR assay. The FX1574 *ubql-1(tm1574)* strain was obtained from the Shared Information of Genetic Resources (SHIGEN; http://shigen.nig.ac.jp/shigen/index.jsp) Center of Genetic Resource Information, National Institute of Genetics, Mishima, Japan, and the presence of the *(tm1574)* allele was confirmed via genotyping PCR. All strains were backcrossed 4 generations to ancestral N2 and had an uncompromised health status. Worms were not involved in previous procedures and test naive.

Cell culture, chemical treatment and radiation

Human dermal fibroblast (HDF) lines were established from skin biopsies and authenticated by validating the UBQLN4 c.976C > T mutation. Sex of HDF cell lines: patient A-IV-4 male; patient A-IV-5 female; patient B-IV-3 male; parent B-III-2 male; WT_1 male; WT_2 female. HDFs as well as U2-OS (sex: female), MDA-MB-231 (sex: female) and HEK293FT (sex: female) cells were grown in DMEM with 10% fetal bovine serum at 37°C in 5% CO_2 atmosphere. Neuroblastoma cell lines CHP212 (sex: male), Kelly (sex: female), BE(2)C (sex: male), Lan5 (sex: male), IMR32 (sex: male), Lan-1 (sex: male), CHP134 (sex: male), SHEP (sex: female), SKNAS (sex: female), CLB-GA (sex: male), SY5Y (sex: female) and GIMEN (sex: female) were grown in RPMI-1640. Neuroblastoma cell lines SKNDZ (sex: female) and NMB (sex: female) were grown in DMEM; SK-N-SH (sex: female) was grown in Modified Eagle Medium (MEM, ThermoFisher Scientific, Waltham MA, USA) and NBL-S (sex: male) was grown in Iscove's Modified Dulbecco's Medium (IMDM, ThermoFisher Scientific, Waltham MA, USA). Medium for all neuroblastoma cell lines contained 10% fetal bovine serum and cells were grown at 37°C and 5% CO_2. All commercially available cell lines were not further authenticated. The DNA-PK inhibitor, KU60648, the ATM inhibitor, KU60019, the ATR inhibitor AZ20, the PARP1 inhibitor olaparib and the MRE11 inhibitors Mirin and PFM01 were diluted in DMSO prior to addition to the culture medium. Cells were irradiated using an X-ray instrument (model 160HF, Philips, Germany), or treated with NCS, hydroxyurea, cisplatin, camptothecin or etoposide.

METHOD DETAILS

Whole-exome sequencing

Genomic DNA was extracted from peripheral blood using standard methods. For library preparation, 1 μg of DNA was fragmented by adaptive focused acoustics on a Covaris S220 (Covaris Inc, Woburn, MA, USA) for 60 s with a duty cycle of 10%, intensity of 5, and 200 cycles per burst. Library was generated on fragmented DNA using TruSeq Sample Preparation Kit v2 (Illumina) following low-throughput and gel-free method protocols. Exome enrichment of library fragments was performed with the NimbleGen Human SeqCap EZ v3.0 Kit (Roche, CA, USA) following the manufacturer's protocol and under consideration of the technical note ''Targeted sequencing with NimbleGen SeqCap EZ Libraries and Illumina TrueSeq DNA samples Prep Kit'' released by NimbleGen. All samples were analyzed on a Bioanalyzer using the Agilent DNA 1000 kit (Agilent, CA, USA) prior to sequencing on an Illumina HiSeq2000 platform using the paired-end sequencing protocol. 100 bp paired end reads were aligned to the human reference genome (GRCh38/hg38) using the Burrows-Wheeler Aligner (BWA 0.7.15) and PCR-duplicate marking was performed with Picard (v. 1.84). Indel realignment, base quality recalibration and variant calling were performed using the Genome Analysis ToolKit (GATK 3.7) and annotation with Annovar (version 2016-02-01 using the RefSeq gene definitions and the frequency of the variants in the following databases: ExAC (Exome Aggregation Consortium, v. 0.3), gnomAD (genome Aggregation Database, v. 2.0), Kaviar (Known VARiants, v. 160204-Public), hrcr1 (halotype reference consortium), and gme (Great Middle East). Variants with a frequency in any database of > 1% or present in our inhouse database in more than two distinct phenotypes were excluded. Variants further than 10 bp form the exon/intron boundaries and exonic variants not predicted to affect protein sequence were also excluded. Finally, variants not present in both datasets, heterozygous variants and hemizygous variants were also excluded.

RNA sequencing

Libraries were prepared using the Illumina TruSeq stranded mRNA sample preparation Kit. Starting with 1 μg of total RNA, poly-A selection (using poly-T oligo-attached magnetic beads) followed, and mRNA was purified and fragmented using divalent cations under elevated temperature. RNA fragments underwent reverse transcription using random primers followed by second strand cDNA synthesis using DNA Polymerase I and RNase H. After end repair and A-tailing, indexing adapters were ligated. The products were purified and amplified (14 PCR cycles) to create the final cDNA libraries. After library validation and quantification (Agilent Tape Station), equimolar amounts of the libraries were pooled. The pool was quantified using the Peqlab KAPA Library Quantification Kit and the Applied Biosystems 7900HT Sequence Detection System. The pool was sequenced in an Illumina HiSeq 4000 sequencer with a paired-end (2x75nt) protocol. Raw sequencing reads were mapped to the reference genome (hg19) using the Star aligner, and FPKM expression values were computed based on the refSeq reference transcriptome. Splice junctions between exon 5 and 7 of *UBQLN4* were extracted from the alignments (spliced reads) and normalized to the coverage of the corresponding exons. Finally, the relative proportion of the splice junctions of exon 5-6, 6-7, and 5-7 were determined.

Vector constructs

Full-length UBQLN4 cDNA cloned in pCDNA3.1 was received from Vivian Su (University of Hawaii at Maona), PCR amplified, and cloned into pLNCX2 (Clontech, Mountain View, CA) using MluI and NotI restriction sites. FLAG or eGFP were PCR amplified and cloned n-terminal using BglII and MluI restriction sites. GFP.UBQLN4.S318A mutant cDNA was generated by introducing a point mutation (T952G) and GFP.UBQLN4.S318D mutant cDNA was generated by introducing two point mutations (T952G, C953A) utilizing the QuickChange II Site-Directed Mutagenesis Kit (Agilent, CA, USA). The GFP.UBQLN4ΔUBL construct was obtained by deleting the N-terminal 89 amino acid residues from the protein. The GFP.UBQLN4ΔUBA construct was obtained by deleting the C-terminal 44 amino acid residues from the protein.

Retroviral and lentiviral vector production

HEK293FT cells were plated into 10 cm dishes in DMEM + 10% FCS, and 24 hr later were co-transfected with pMDLg/pRRE and pMD2.G packaging plasmids and pLNCX2 expression plasmids encoding various UBQLN4 constructs or empty vector using $CaCl_2$ transfection. Briefly, cells were seeded to a confluency of 50%–70%. 500 μl 250 mM $CaCl_2$ solution were added into an Eppendorf tube as well as 10 μg of vector. Afterward, 500 μl 2x HEBS buffer were added dropwise while vortexing the solution thoroughly. The solution was then added dropwise onto the cells. The next day, medium was changed to DMEM + 20% FCS. Cell culture supernatants were collected 24, 48 and 72 hr later, centrifuged at 300 g for 5 min and sterile filtered. Using these viral supernatants, HDFs or U2-OS cells were transduced in the presence of 8 μg/ml polybrene for 24 hr and subsequently selected with G418. For RNAi-mediated gene silencing, replication-incompetent lentiviruses were produced with pLKO.1-Puro based vectors, which expressed specific shRNAs targeting UBQLN4. For that purpose, HEK293FT cells were co-transfected with pRSV-Rev, pMDLg/pRRE and pCMV-VSV-G packaging and envelope plasmids and pLKO.1 expression plasmids. Supernatants were collected after 24, 48 and 72 hr, centrifuged at 300 g for 5 min and sterile filtered. U2-OS cells were transduced with these viral supernatants in the presence 8 μg/ml polybrene for 72 hr (3 cycles of transfection) and selected using puromycin. Finally, knockdown efficiency was confirmed by immunoblotting.

RNA Interference

Cells were grown to 50% confluence and transfected with respective siRNA (UBQLN4, CTIP, Control) using DharmaFECT1 transfection reagent (Dharmacon Inc.). For that purpose, diluted siRNA (tube 1) and DharmaFECT1 transfection reagent (tube 2) were added to separate tubes containing serum-free medium and incubated for 5 min at room temperature. Subsequently, contents of tube 1 were added to tube 2 and incubated for 20 min at room temperature and distributed onto respective cell culture dishes. Cells were then incubated at 37°C in 5% CO2 for 48-96 hours for further downstream experiments.

Generation of CRISPR-Cas9 knockout cell lines

Specific CRISPR guides were designed for DNA sequences within exon 1 (CGATCGAGCCTCGGTCAAGG) and exon 6 (AGAAGGG ATTGTTGCCAAAC) of the *UBQLN4* gene using MIT web tool for CRISPR guide selection (http://zlab.bio/guide-design-resources). The sequences for specific and non-targeting crRNA and trRNA were dissolved in 10 mM Tris-HCl, pH7.4. Thirty to fifty thousand cells of MDA-MB-231-Cas9 were plated and transfected using 50 nM of each crRNA and trRNA (GE Healthcare Dharmacon, CO, USA). After 48 hr the medium was changed and the cells were grown to confluence. Knockout was confirmed by immunoblotting.

Immunoblotting and chemical fractionation

Cell lysates were obtained by lysing washed cells with RIPA buffer (50 mM Tris HCl pH 7.5, 150 mM NaCl, 1% NP40, 0.5% Sodium deoxycholate monohydrate, 0.1% SDS, 2.5 U Benzonase, 200 mM Mn^{2+}) containing protease inhibitor cocktail and incubated head-over tail at 4°C for 60 min. Cell lysates were clarified by centrifugation and the protein concentration was quantified using the Bradford assay. Lysates were separated using SDS-PAGE and transferred onto nitrocellulose (0.2 μM) or PVFF membranes (0.45 μM). Membranes were blocked in 5% BSA-TBST. Membranes were reacted with primary antibodies, washed four times, 5 min each with 0.1% Tween-20 (pH 7.6), and subsequently incubated with peroxidase-conjugated secondary antibodies. Chemiluminescence was performed using Clarity Western ECL Substrate. For cellular fractionation experiments, U2-OS cells were chemically fractioned using a subcellular protein fractionation kit (Thermo Fisher Scientific, USA). For that, cells were harvested with trypsin-EDTA, centrifuged at 500*g* for 5 min and washed with ice-cold PBS. After adding CEB buffer to the cell pellet, the tube was incubated at 4°C for 10 min with gentle mixing. Following centrifugation at 500*g* for 5 min the supernatant (cytoplasmic extract) was transferred to clean pre-chilled tube on ice. Next, MEB buffer was added to the pellet, the tube briefly vortexed and incubated at 4°C for 10 min with gentle mixing. The tube was then centrifuged at 3000*g* for 5 min and the supernatant (membrane extract) transferred to a clean pre-chilled tube on ice. NEB buffer was added to the pellet, vortexed on the highest setting for 15 s. Following an incubation at 4°C for 30 min with gentle mixing, the tube was centrifuged at 5000*g* for 5 min and the supernatant (nuclear extract) transferred to a clean pre-chilled tube on ice. Lastly, room temperature NEB buffer containing Micrococcal Nuclease and $CaCl_2$ was added to the pellet, vortexed for 15 s and incubated at room temperature for 15 min. After incubation, the tube was centrifuged at 16,000*g* and the supernatant (chromatin-bound nuclear extract) transferred to a clean pre-chilled tube on ice.

Cell viability measurement

Cell lines were plated into 96-well plates at densities of 5000-10000 cells/well. 24 hr later, cells were treated with various doses of genotoxic chemicals for 96 hr. After the incubation, room-temperature CellTiter-Glo® Reagent (Promega, USA) was added 1:1 to each well and the plates were incubated at room temperature for 10 min. Luminescence was measured with the Tecan Infinite M1000 Pro (Tecan, Männedorf, CHE) and normalized against control cells treated with vehicle solution.

Clonogenic survival assay

U2-OS cells were plated in triplicate at densities of 100–3000 cells per 60 mm plate and incubated for 24 hr before exposure to various NCS doses. Two weeks later cell colonies were fixed and stained with 0.2% crystal violet in 50% ethanol and counted under a dissection microscope.

Cleaved caspase-3 measurement

U2-OS cells were harvested and washed with 1 mL of ice-cold PBS. Fixation was performed by adding 1 mL of ice-cold 100% methanol slowly while gently vortexing. After 10 min, cells were washed three times with 1 mL of PBS + 0.5% BSA, and anti-cleaved caspase-3 (Asp175) was added. Cells were incubated for 2 hr at room-temperature, washed and incubated with secondary Alexa Fluor 488 in the dark for 1hr and washed three times with 1 mL of PBS + 0.5% BSA. Sorting was performed using a Beckman Coulter Gallios flow cytometer at 50.000 events/ sample and analyzed with the software Kaluza (Beckman Coulter).

Comet assay

Cells were treated with DNA damaging agents, harvested, and the comet procedure was applied using the CometAssay experimental system (Trevigen). For that, cells were mixed with low-melting agarose and the cell suspension was overlaid on microscope slides. Cell lysis was carried out within the agarose. After lysis, electrophoresis of the DNA trapped in the agarose was performed at 1 V/cm for 30 min. After staining the slides with SYBR Green dye for 10 min, images of 100 randomly selected cells per sample were captured using a Nikon eclipse 55i fluorescent microscope and digital fluorescent images were obtained by using the NIS-elements AR software. The relative length and intensity of DNA tails relative to heads is proportional to the amount of DNA damage in individual nuclei.

These parameters were measured observer-independent and in an unbiased fashion by tail moment quantification with TriTek Comet Score software (TriTek Corp., Sumerduck, VA). Exemplary images of single cells from comet slide samples were obtained post analysis.

DSB repair pathway assays

U2-OS cells bearing a single-copy integration of the reporters DR-GFP (Gene conversion), or SSR (NHEJ:HR) were used to analyze the different DSB repair pathways (López-Saavedra et al., 2016). In both cases, 4.000 cells were plated in 96-well plates. One day after seeding, cells were transfected with the indicated siRNA or infected with retroviral particles carrying the indicated plasmids. The medium was changed after 6-8 hr. The following day, cells were infected with a lentivirus harboring I-SceI and labeled with BFP at a multiplicity-of-infection of 10 (López-Saavedra et al., 2016). After 24 hr, cells were washed with fresh medium and maintained during an additional 24 hr. Cells were then fixed with 4% paraformaldehyde, stained with Hoechst 33,432, and washed with PBS before visualization with a fluorescent microscope for blue, and in the case of SSR, green and red fluorescence. The repair frequency was calculated as the percentage of blue cells expressing GFP for the DR-GFP. For the NHEJ:HR balance, the ratio between green versus red cells in each condition was calculated. To facilitate the comparison between experiments, this ratio was normalized with siRNA or an empty vector control. Conditions that skewed the balance toward increased NHEJ repair resulted in a fold increase above 1. In contrast, a net decrease of this ratio (for example, values below 1) represented an imbalance of SSR toward HRR. Data represent a minimum of four sets of triplicate experiments. Statistical significance was determined using the paired sample t test.

Single Molecule Analysis of Resection Tracks

Single Molecule Analysis of Resection Tracks (SMART) was performed as previously described (Cruz-García et al., 2014). For that purpose, U2-OS cells transfected with siRNA against UBQLN4, a control siRNA, UBQLN4.FLAG, UBQLN4.S318A.FLAG or empty-vector FLAG construct were cultured in the presence of 10μM bromodeoxyuridine (BrdU) for 24 hr, irradiated with 10 Gy of IR and harvested 1 hr later. Cells were embedded in low-melting agarose and in-gel DNA extraction followed. To stretch the DNA fibers, silanized coverslips were dipped into the DNA solution for 15 min and pulled out at constant speed (250μm/s). Coverslips were baked for 2 h at 60°C and incubated without denaturation with an anti-BrdU mouse monoclonal antibody. After washing with PBS, coverslips were incubated with a secondary antibody. The coverslips were mounted with ProLong® Gold Antifade Reagent (Molecular Probes, Oregon, USA) and stored at −20°C. DNA fibers were observed using a Nikon NI-E microscope under a PLAN FLOUR40 × /0.75 PHL DLL objective. The images were recorded and processed using NIS ELEMENTS Nikon software. For each experiment, at least 200 DNA fibers were analyzed, and the length of DNA fibers was measured using Adobe Photoshop CS4 Extended version 11.0 (Adobe Systems Incorporated). Experiments were repeated independently four times. Statistical significance in these experiments was determined with the paired Student's t test.

Laser microirradiation and imaging of cells

U2-OS cells expressing ectopic, GFP-tagged proteins were plated on glass bottom dishes (MatTek, Ashland, MA) and pre-sensitized with 10 μM BrdU for 48 hr. The dishes were transferred into a microscope top-stage incubator equipped with a control system for gas mixture and humidity (Okolab, Ottaviani, Italy). DNA damage was induced on a Leica TCS SP8 confocal microscope (Leica Microsystems, Wetzlar, Germany) using a 405 nm diode laser focused through an HC PL APO 63X, 1.4-numerical aperture oil immersion objective (8% laser power, scan speed 650 msec, 40 scans). Images were acquired using the same system.

Relocalization of endogenous proteins to sites of laser-induced DNA damage was followed by immunostaining. DNA damage was induced using two-photon-based micro-irradiation obtained from an 800 nm laser beam in an LSM 510 Meta confocal microscope (Carl Zeiss, Jena, Germany). The microscope was equipped with a Spectral-Physics Mai-Tai (Deep-See) multi-photon laser system focused through a 63 × 1.25 numerical aperture oil immersion objective. Microirradiation was carried out at 8% laser power and scan speed of 1.61 μsec, with 40 repetitions at zoom × 1. A Leica TCS SP8 confocal microscope was used for imaging. In order to visualize UBQLN4 and 53BP1 laser stripes, cells were washed with PBS and incubated for 3 min at room temperature with CSK buffer containing 10 mM PIPES, pH 7.0, 100 mM NaCl, 300 mM sucrose, 3 mM $MgCl_2$, and 0.7% Triton X-100. The cells were then washed in PBS and incubated for another 3 min in CSK buffer supplemented with 0.3 mg/ml RNase A. The above described immunofluorescence protocol was then followed.

Immunostaining and fluorescence measurements

HDFs were seeded onto 96 well plates for immunofluorescence assays. For RAD51 stainings, cells were additionally pre-extracted in sucrose buffer (25 mM HEPES pH 7.5, 50 mM NaCl, 1 mM EDTA, 3 mM $MgCl_2$,300 mM Sucrose, 0.5% Triton-X) for 2 min on ice. Cells were fixed for 10 minutes in room temperature with 4% Paraformaldehyde, followed by three washes with ice-cold 1x PBS. Subsequently, the cells were blocked for 60 min at room temperature in PBS containing 5% normal goat serum (NGS), 2% bovine serum albumin and 0.01% Triton X-100. Incubation with the primary antibody was performed over night at 4°C. Incubation with the secondary antibody was performed for 1 h at room temperature. Analysis was performed as described in "High-content screening microscopy." In contrast, U2-OS cells were fixed and stained on regular coverslips. Cleaved caspase 3 intensity and nuclear foci of γH2AX in U2-OS cells were quantified using ImageJ software (with the PZfociEZ plugin for γH2AX nuclear foci).

High-content screening microscopy

High-content screening (HCS) microscopy was performed on HDFs using a Thermo Fisher Cellomics ArrayScan XTI with LED light source. Images of 1104 × 1104 pixels were acquired with a 20x objective (Zeiss) and analyzed using the Cellomics software package (Colocalization V.4 Bioapplication). Images were background corrected (3D surface fitting) and DAPI stained cell nuclei were identified according to the object selection parameters size: 100–1500 μm^2, ratio of perimeter squared to 4π area: 1–2, length-to-width ratio: 1–5, average intensity: 400–4000, total intensity: 4×10^6–2×10^7. Foci of γH2AX, MRE11, RPA70, RAD51 and Ubiquitin intensities were quantified within the nuclear region at another excitation wavelength (485 ± 20 nm or 650 ± 20nm). Object selection parameters for foci were size: 0.1–10 μm^2, ratio of perimeter squared to 4π area: 1–5, length-to-width ratio: 1–5, average intensity: 500–10000, total intensity: 300–2×10^6. To determine the cell cycle stage, we analyzed the distribution of the total DAPI intensity using a custom R script. Four thresholds were adjusted manually to gate cells in 2N (G0/G1), 2-4N (S), and 4N (G2/M) stages, respectively. Cells in the G0/G1 phases possess a normal diploid DNA content (2N) whereas cells in G2/M contain exactly twice this amount (4N). As DNA is synthesized during S-phase, cells are found with a DNA content ranging between 2N and 4N. The gates were then applied to evaluate the mean number of foci in cells of the respective cell cycle stage. Single cell data were further processed and plotted using R packages. High content screening kinetic experiments were analyzed with R using ordinary two-way ANOVA. HCS microscopy results are means ± standard deviation; n = 3-4 wells; > 2000 cells/well; two-way ANOVA with Bonferroni's test. *$p < 0.05$; **$p < 0.01$; ***$p < 0.001$.

Immunoprecipitation

For GFP-Trap and FLAG-IP experiments, 293FT cells were transfected with respective plasmids, treated and harvested. Cells were then incubated in lysis buffer (150 mM NaCl, 50 mM Tris HCl pH 7.5, 2 mM $MgCl_2$, 1% NP40 and EDTA-free protease inhibitor cocktail) for 60 min with rotation at 4°C. For the identification of ubiquitin-dependencies 10 mM *N*-Ethylmaleimide (NEM) was added to the lysis buffer. The resultant cell lysates were pre-cleared at 15.000 g at 4°C for 20 min. Lysates were incubated with GFP-Trap agarose beads or FLAG-M2 agarose beads at 4°C for 3 hr. The resulting complexes were washed with wash buffer (150 mM NaCl, 50 mM Tris HCl pH 7.5, 0.5% NP40 and complete protease inhibitor cocktail) and analyzed by SDS-PAGE. In the case of HIS immunoprecipitations, Ni-NTA magnetic beads were added to lysates also containing 15 mM Imidazole, 5 mMTris-(2-carboxyethyl)-phosphin (TCEP) and incubated overnight at 4°C with gentle agitation. Beads were washed 5 times with IP wash buffer (20 mM HEPES pH 7.9, 300 mM NaCl, 10% Glycerol, 0.1% NP-40, 5mM TCEP, 15 mM Imidazole, 10mM NEM) and eluted in elution buffer (20 mM HEPES pH 7.9, 300 mM NaCl, 10% Glycerol, 0.1% NP-40, 5 mM TCEP, 200 mM Imidazole). In the case of USP2 treatment, 20 µl USP2 buffer (35 mM HEPES pH 7.9, 75 mM NaCl, 1 mM DTT) and 50 µM USP2 were added to the sample and the sample was incubated for 30 min at 37°C with gentle agitation.

LC-MS/MS phosphorylation analysis

Cell lysates were precipitated with acetone and resuspended in 8 M Urea. After reduction with DTT and carbamidomethylation with IAA, proteins were digested overnight at 37°C, using the proteases LysC (Wako) and, after dilution with 50 mM potassium phosphate buffer pH 5.8, trypsin (Promega) and GluC (Promega). Samples were desalted using SepPak C18 cartridges (Waters) and phosphorylated peptides enriched with the High-Select TiO2 Phosphopeptide Enrichment Kit (Thermo Fisher). Proteomic analysis was performed using an Easy nLC 1200 UHPLC coupled to a QExactive HF-X mass spectrometer (Thermo Fisher). Peptides were resuspended in Solvent A (0.1% FA), picked up with an autosampler and loaded onto in-house made 50 cm fused silica columns (internal diameter (I.D.) 75 µm, C18 1.7 µm, Dr. Maisch beads) at a flow rate of 1.5 µL/min. A 90 min segmented gradient of 4%–55% Solvent B (80% ACN in 0.1% FA) over 81 min and 55%–95% Solvent B over 9 min at a flow rate of 250 nL/min was used to elute peptides. Eluted peptides were sprayed into the heated transfer capillary of the mass spectrometer using a nano-electrospray ion source (Thermo Fisher Scientific). The mass spectrometer was operated in a data-dependent mode, where the Orbitrap acquired full MS scans (350-1650 m/z) at a resolution (R) of 60,000 with an automated gain control (AGC) target of 3×10^6 ions collected within 20 ms. The dynamic exclusion time was set to 20 s. From the full MS scan, the 15 most intense peaks ($z \geq 2$) were fragmented in the high-energy collision-induced dissociation (HCD) cell. The HCD normalized collision energy was set to 28%. LC-MS/MS scans with an ion target of 1.5×10^5 ions were acquired with R = 30,000, with a maximal injection time of 54 ms and an isolation width of 1.3 m/z. The raw files were processed using MaxQuant software (version 1.5.3.8) and its implemented viewer and Andromeda search engine (Cox et al., 2011). Parameters were set to default values and Phospho (STY) was added as variable modification. Intensities were scaled to mean of zero and unit variance for separate measurements. Graphs were generated and two-sided t test.

Histological analysis

Formalin-fixed paraffin-embedded (FFPE) nevus and melanoma samples were cut into 4µm thick sections and mounted on slides. After UBQLN4 staining, samples were assessed and the H-score calculated.

Measurement of *C. elegans* HRR efficiency

Worms were synchronized at late L4 stage by picking and were kept for 24 hr at 20°C until reaching adulthood. For each condition, 5 adult worms were transferred to 35-mm NGM plates seeded with a drop of OP50 and allowed to lay eggs for a time period of 2 hr at 20°C. Animals were then removed from plates and eggs were immediately irradiated with 0, 20 or 40 Gy of γ-irradiation. 24 hr later,

numbers of hatched and non-hatched eggs were counted and percentages of embryonic survival were calculated. Each experiment was performed in biological triplicates.

C. elegans immunofluorescence staining

Wt and *ubql-1(tm1574)* mutants were synchronized at L4 larval stage by picking and kept at 20°C. 24 hr later worms were either exposed to 90 Gy of γ-irradiation using a BIOBEAM 8000 with Cs137 radionucleotide source, or were left untreated to serve as negative controls. Worms were kept another 24 hr at 20°C before being dissected with syringe needles to expose germlines. Tissues were fixed for 5 min with 4% paraformaldehyde solution on adhesive HistoBond®+ slides (Paul Marienfeld GmbH & Co. KG) before freeze cracking on dry ice. Slides were subsequently fixed for 1 min in ice-cold methanol at −20°C and washed 3x in PBS-T followed by a 30 min blocking step with 10% donkey serum in PBS-T. For detection of ubiquitinylated conjugates tissues were incubated overnight at 4°C with monoclonal FK2 antibody (Merck Millipore; Dilution: 1:500 in 10% donkey serum in PBS-T). The next day, slides were washed 3x in PBS-T and exposed to secondary antibody (AlexaFluor 488 Donkey anti-Mouse IgG; Dilution: 1:500 in 10% donkey serum in PBS-T) for 2 hr at room-temperature in the dark. After 3 final washes in PBS-T, slides were mounted with a drop of DAPI Fluoromount-G® (SouthernBiotech) and sealed with nailpolish. Images of five individual germlines per condition were taken using a Zeiss Meta 710 confocal microsope. Images were subsequently processed and analyzed using the ImageJ software package.

QUANTIFICATION AND STATISTICAL ANALYSIS

Statistical analyses were performed using the GraphPad Prism software package. The type of statistical analyses, parameters and number of replicates are indicated for each experiment in the figure legends. For all tests, p value significance was defined as follows: not significant (n.s.) $p > 0.05$; *$p < 0.05$; **$p < 0.01$; ***$p < 0.001$.

DATA AND SOFTWARE AVAILABILITY

The mass spectrometry proteomics data have been deposited to the ProteomeXchange Consortium via the PRIDE partner repository with the dataset identifier PXD011488. High-content screening (HCS) microscopy raw data has been deposited to the Mendeley repository under https://doi.org/10.17632/gz4xvwbvhs.1.

A

	A-IV-4	A-IV-5
total variants	400773	1561381
low frequency	24134	66808
affecting protein	513	543
homozygous	31	40
shared	8	
truncating	1	

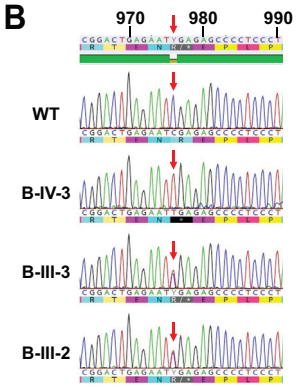

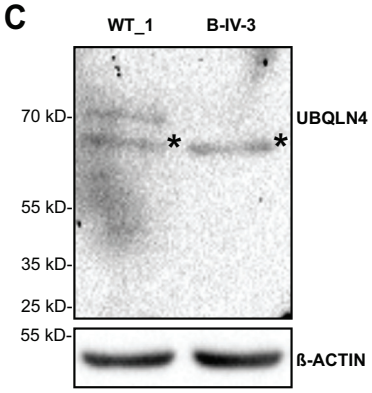

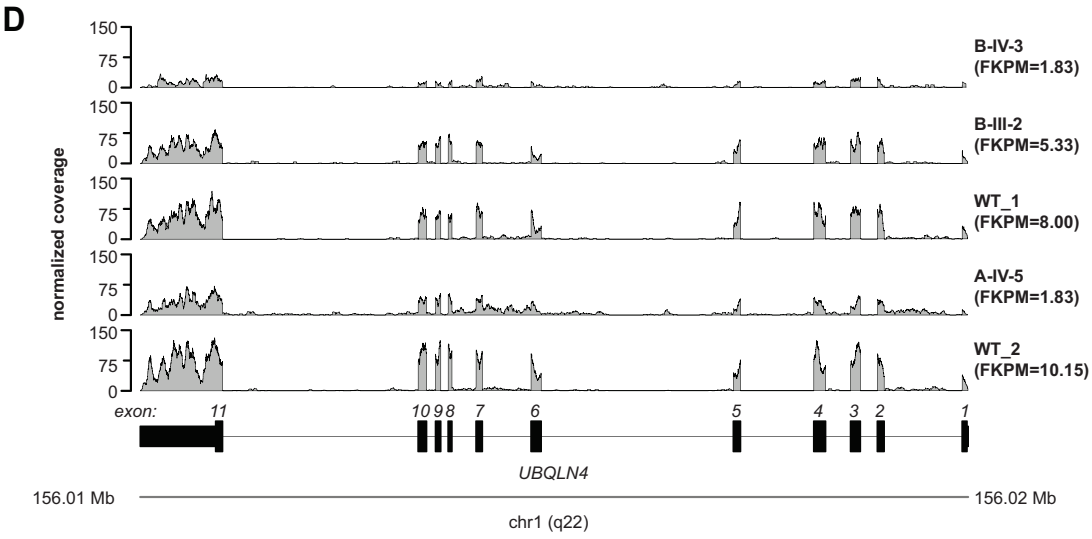

E

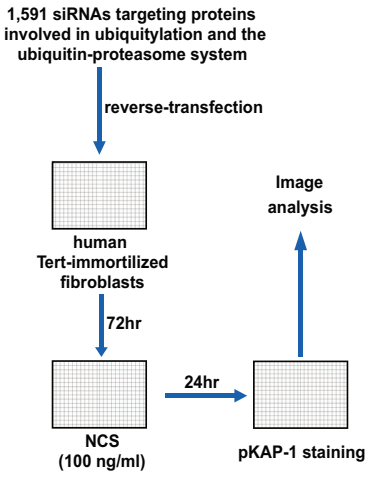

F

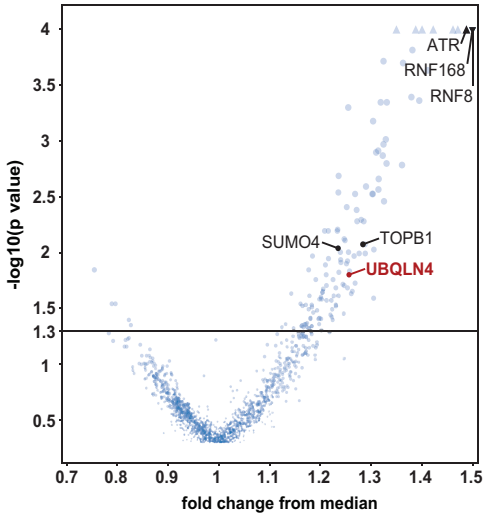

(legend on next page)

Figure S1. Homozygous c.976C > T Mutation in the *UBQLN4* Gene Leads to UBQLN4 Deficiency Syndrome, Related to Figures 1 and 2

(A) Number of variants remaining after each filtering step.

(B) Genomic sequencing of lymphocyte DNA obtained from a healthy control, patient *B-IV-3*, and carriers *B-III-2* and *B-III-3*. The arrow indicates the location of the c.976C > T mutation.

(C) Lysates of WT and DMFs derived from patient *B-IV-3*, subjected to immunoblotting with an n-terminal anti-UBQLN4 antibody. The asterisks mark an unspecific band.

(D) Normalized *UBQLN4* transcriptome sequencing coverage for cell lines derived from patients *A-IV-5* and *B-IV-3*, the carrier *B-III-2* and wt controls (WT_1 and WT_2). Gene expression of *UBQLN4* is represented by FPKM values (fragments per kilobase of exon per million fragments mapped).

(E) High throughput screen for DDR factors in the ubiquitin arena (Baranes-Bachar et al., 2018). Human Tert-immortalized fibroblasts seeded in 384-microwell plates were reverse-transfected with siRNAs representing 1591 siRNA pools targeting mRNAs of various proteins that are involved in protein ubiquitylation and the ubiquitin-proteasome system. 72hrs later, cells were treated with 100 ng/ml NCS, and 24 hr later fixed and stained with an antibody against phospho-KAP-1.

(F) Quantitative data from 3 experimental repeats were normalized and plotted as fold change from median in respect to p value. p values were converted directly from Z-scores and were not corrected for multiple testing, as UBQLN4 was specifically looked at in an exploratory setting. Upward triangles indicate p values < 0.0001; tilted triangles indicate p values < 0.0001 and fold change from the median > 1.5.

Patient A-IV-4

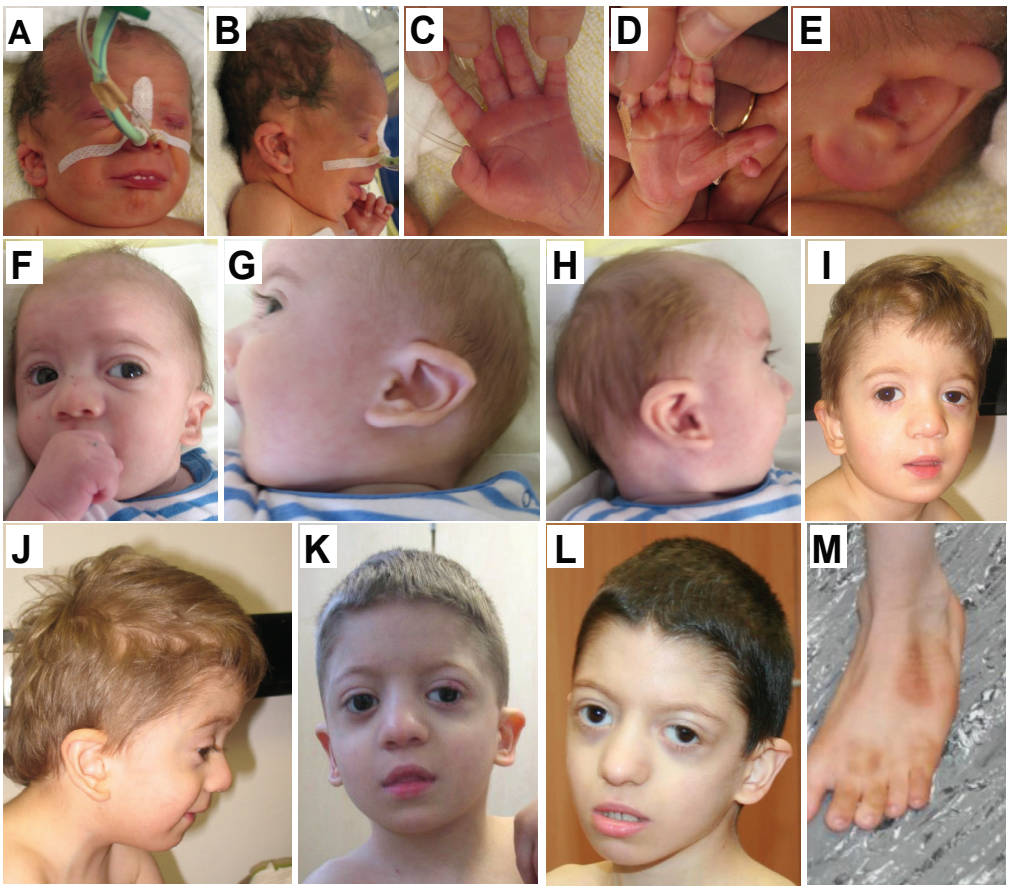

Patient B-IV-3

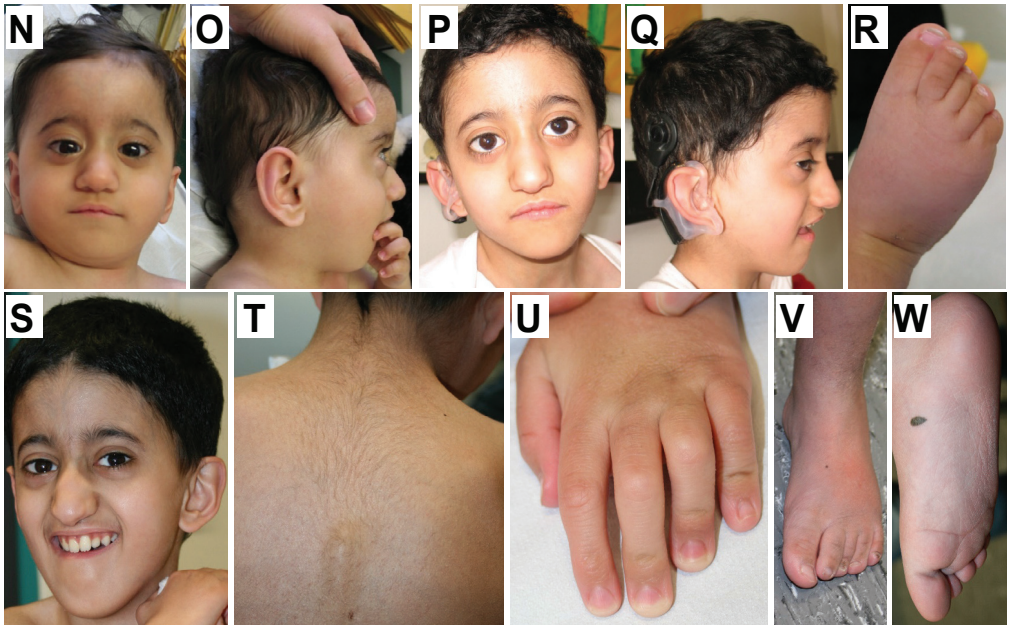

(legend on next page)

Figure S2. Images Displaying Patients A-IV-4 and B-IV-3, Related to Figure 1

(A-H) Patient *A-IV-4* shortly after birth with low-set and posteriorly rotated ears, right preaxial polydactyly and bilateral simian creases.

(I-K) Patient *A-IV-4* at the age of 5 $^{4}/_{12}$ years presenting with proptosis, prominent nose and micrognathia.

(L-M) Patient *A-IV-4* at the age of 11 years presenting with dystrophic habitus, hypertelorism, downward slanting palpebral fissures, proptosis, long nose, small mouth, feet brachydactyly and hyperpigmented areas.

(N and O) Patient *B-IV-3* at the age of 17 months with proptosis, micrognathia and low-set ears.

(P-R) Patient *B-IV-3* at the age of 6 years, presenting with hypertelorism, large nose, an underriding and hypoplastic third toe.

(S-W) Patient *B-IV-3* at the age of 10 years, with large nose, short philtrum, camptodactyly of fingers III to V, dark nevi on the right foot, dorsal hirsutism, pes adductus and dystrophic habitus.

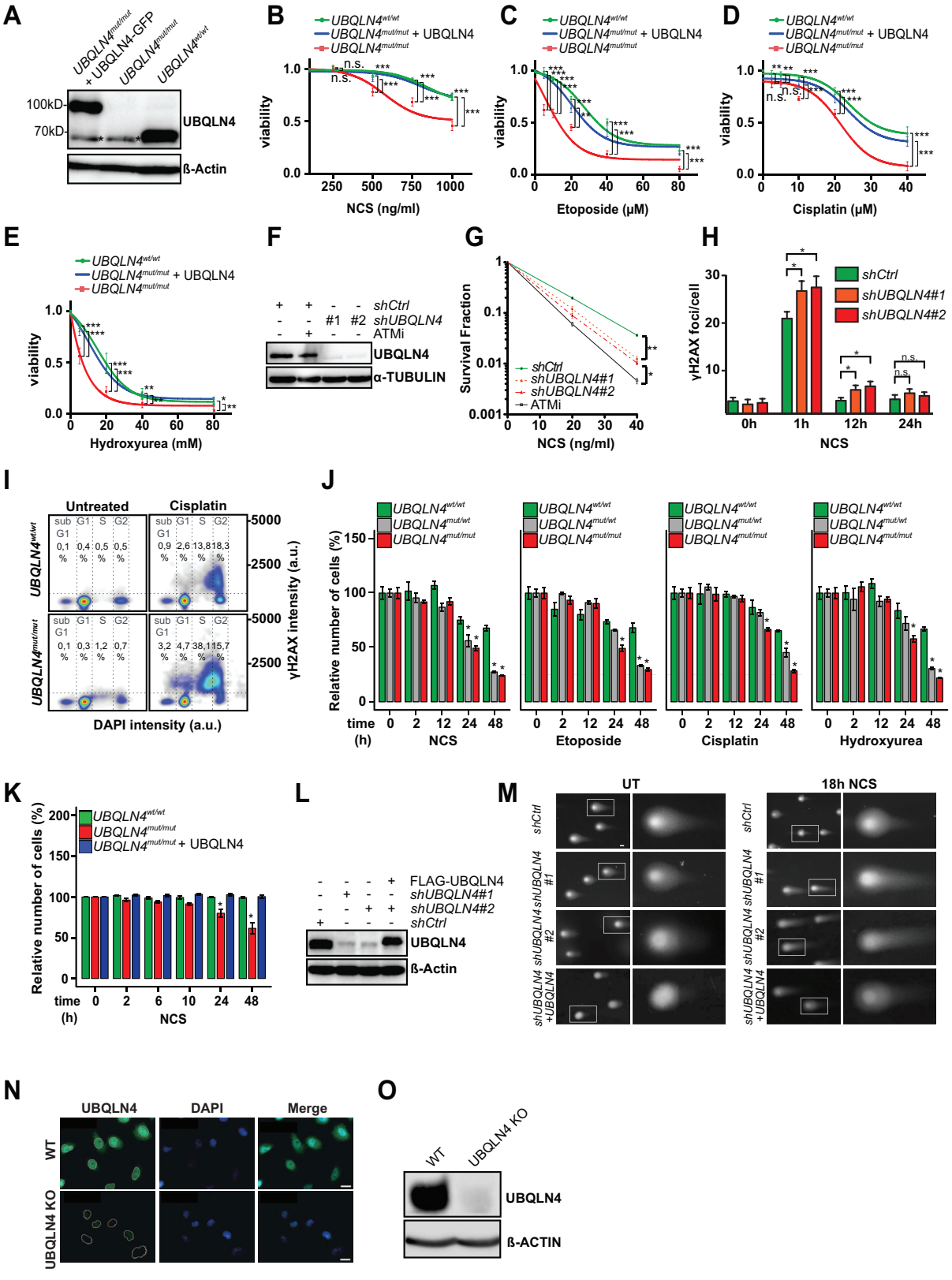

(legend on next page)

Figure S3. Loss of UBQLN4 Increases Cellular Sensitivity to Genotoxic Agents, Related to Figure 2

(A) Immunoblot displaying the expression level of UBQLN4 of cell lines used in (B-E). The asterisks mark an unspecific band.

(B-E) Intracellular ATP was measured as a surrogate marker for cell viability. Cells with the indicated genotypes were treated with NCS (B), etoposide (C), cisplatin (D) or HU (E) for 96 hr and ATP levels were measured. Dose response curves were generated with error bars displaying the standard deviation of the mean of three independent experiments. p values were calculated using the t test with Welch's correction not assuming equal variance. $p < 0.05$ (*); $p < 0.01$ (**); $p < 0.001$ (***).

(F) Immunoblot depicting UBQLN4 expression levels of cells used in (G).

(G) Clonogenic survival curve of U2-OS cells transduced with two shRNAs directed against UBQLN4 and subsequently treated with various NCS doses. *shControl* transduced cells and cells treated with ATM inhibitor KU-60019 (ATMi, 5μM) served as negative and positive controls, respectively. Error bars represent the standard deviation of the mean of n = 3 experiments. p values were calculated using the t test with Welch's correction not assuming equal variance. $p < 0.05$ (*); $p < 0.01$ (**).

(H) Number of γH2AX nuclear foci in U2-OS cells treated with 50 ng/ml of NCS at the indicated time points. Cells were transduced with control shRNA (shCtrl) or two shRNAs directed against UBQLN4. Error bars represent the standard deviation of 1000 cells analyzed in 3 independent experiments. Statistical significance was determined with the paired Student's t test. $p < 0.05$ (*).

(I) γH2AX intensity was measured throughout the cell cycle in cells with the indicated genotype following cisplatin treatment. Cell cycle analysis was performed according to DAPI intensity of the nuclei (< 2N = sub G1; 2N = G1; 2-4N = S; 4N = G2). The percentage of γH2AX positive cells within the cell cycle is indicated.

(J) Automated imaging of identical view fields related to Figures 2I–2M allowed the quantification of the relative number of cells observed at the indicated time points and treated with the indicated genotoxic agents. Error bars represent SD of the mean for 3 replicate wells analyzed in one experiment. Easch experiment was carried out twice. Two-way ANOVA with Bonferroni posthoc test, $p < 0.05$.

(K) Automated imaging of identical view fields of the indicated genotypes allowed the quantification of the relative number of cells observed at the indicated time points and treated with 250 ng/ml NCS. n = 3 replicate wells analyzed in three experiments, mean ± SD, Two-way ANOVA with Bonferroni posthoc test, $p < 0.05$ (*).

(L) Immunoblot displaying the expression level of UBQLN4 of cell lines used in Figures 2N and 2O.

(M) Representative images of neutral comet assays related to Figure 2N of NCS-induced (50 ng/ml) DSBs in U2-OS cells transduced with *shControl,* two independent *shUBQLN4* and *shUBQLN4* knockdown cells complemented with ectopic *UBQLN4* cDNA. Scale bar, 10 μm.

(N) Indirect immunofluorescence of MDA-MB-231 *UBQLN4*-KO cells and wt MDA-MB231 cells with anti-UBQLN4 antibody. Scale bar, 10 μm.

(O) Lysates of MDA-MB-231 *UBQLN4*-KO cells and wt MDA-MB231 cells immunoblotted with anti-UBQLN4 antibody.

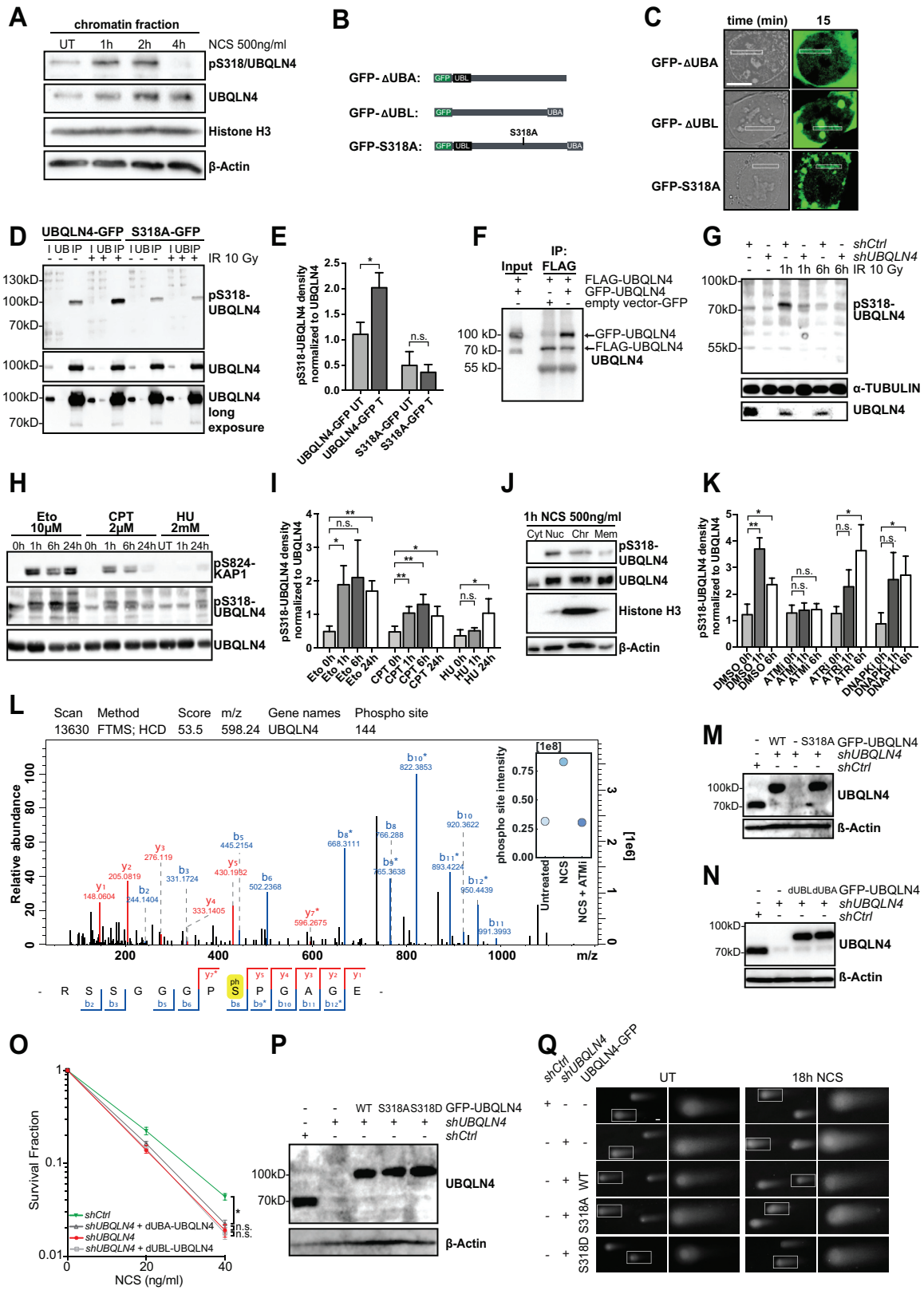

(legend on next page)

Figure S4. ATM-Dependent Phosphorylation of UBQLN4 Mediates DSB Repair, Related to Figure 3

(A) Immunoblot of U2-OS cells treated with 500 ng/ml NCS for the indicated time points. Cell lysates were subsequently fractionated for immunoblotting. Histone H3 served as a positive marker for the chromatin fraction.

(B) Domain diagrams of UBQLN4 mutants.

(C) Recruitment of GFP.UBQLN4ΔUBA, GFP.UBQLN4ΔUBL and GFP.UBQLN4.S318A mutant to sites of DNA damage 15 min after damage induction using a focused laser micro beam. Scale bar, 10 μm.

(D) Immunoblot to demonstrate the detection of S318 UBQLN4 phosphorylation in U2-OS cells using a specific anti-phospho S318 antibody. GFP-tagged UBQLN4 in wt and S318A mutant versions was ectopically expressed in U2-OS cells. At 1 hr after treatment with 10 Gy of IR, ectopic UBQLN4 was immunoprecipitated using an anti-GFP antibody, and the immune complexes were blotted with the indicated antibodies. I = Input; UB = Unbound fraction; IP: Bound fraction. A low-intensity unspecific phosphorylation band is seen in the S318A mutant control IP fraction.

(E) Densitometry analysis of three independent experiments related to (D). Densitometry was quantified by ImageJ of S318-UBQLN4 phosphorylation and normalized to wt UBQLN4. Error bars display the standard deviation of three independent experiments. UT = untreated; T = treated. p values were calculated using the t test with Welch's correction. $p < 0.05$ (*).

(F) Immunoblot to demonstrate dimerization/polymerization of tagged UBQLN4. GFP-tagged and FLAG-tagged UBQLN4 was ectopically expressed in U2-OS cells, ectopic UBQLN4 was immunoprecipitated using FLAG beads and the immune complexes were blotted with UBQLN4 antibody. Empty-vector GFP served as a control.

(G) U2-OS cells transfected with the indicated shRNAs, treated with 10 Gy of IR, and processed for immunoblotting with anti-UBQLN4- and anti-pS318 UBQLN4 antibody at the indicated time points.

(H) Cellular extracts of U2-OS cells were subjected to immunoblotting after treatment with etoposide (Eto), camptothecin (CPT) or hydroxyurea (HU) at the indicated time points. pS824-KAP1 antibody was used as a positive control.

(I) Densitometry analysis of four independent experiments related to (H). Densitometry was quantified by ImageJ of S318-UBQLN4 phosphorylation and normalized to wt UBQLN4. Error bars display the standard deviation of four independent experiments. p values were calculated using the t test with Welch's correction. $p < 0.05$ (*);$p < 0.01$ (**).

(J) U2-OS cells were fractionated (Cyt = cytoplasma; Nuc = nuclear; Chr = chromatin; Mem = membrane) following 1 hr of 500 ng/ml NCS and subjected to immunoblotting. Anti-Histone H3 antibody served as control for the chromatin fraction.

(K) Densitometry analysis of three independent experiments underlying Figure 3E. Densitometry was quantified by ImageJ of S318-UBQLN4 phosphorylation and normalized to wt UBQLN4. Error bars display the standard deviation of three independent experiments. p values were calculated using the t test with Welch's correction. $p < 0.05$ (*); $p < 0.01$ (**).

(L) Selected LC-MS/MS scan of the UBQLN4 peptide with phosphorylated S144 and annotated b- and y-ions. Fragment ions marked with an asterisk (*) result from loss of the phospho- group. Inset top right: LC-MS/MS measured intensities of the phosphorylated S144 site after indicated treatments.

(M) Immunoblot depicting the expression levels of endogenous and ectopic UBQLN4 in cells used for clonogenic survival assays in Figure 3G.

(N) Immunoblot depicting the expression levels of endogenous and ectopic UBQLN4 in cells used for clonogenic survival assays in (O).

(O) Clonogenic survival curve of U2-OS cells transduced with shRNA directed against UBQLN4 (targeting 3′UTR) and mutant forms of UBQLN4 and subsequently treated with various NCS doses. Error bars represent the standard deviation of the mean of n = 3 experiments. p values were calculated using the t test with Welch's correction not assuming equal variance. $p < 0.05$ (*).

(P) Immunoblot displaying the expression level of UBQLN4 of cell lines used in Figure 3H.

(Q) Representative images of neutral comet assays of NCS-induced (50 ng/ml) DSBs in U2-OS cells transduced with either *shControl* or *shUBQLN4* and complemented with UBQLN4-wt, S318A mutant or S318D mutant plasmid related to Figure 3H. Scale bar, 10 μm.

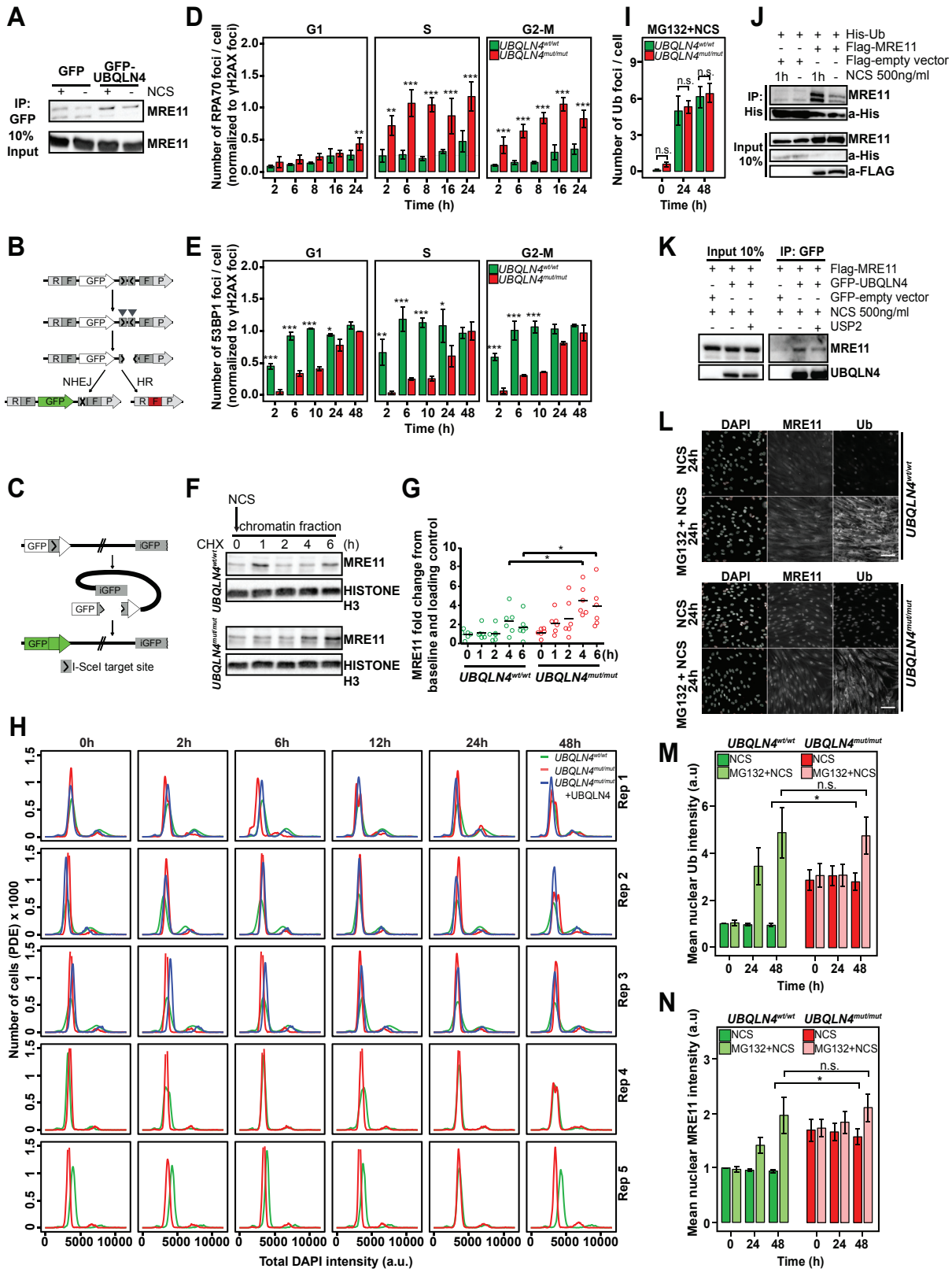

(legend on next page)

Figure S5. Loss of UBQLN4 Leads to Increased HRR and Retention of MRE11, Related to Figures 4 and 5

(A) Immunoblot of MRE11 that co-precipitated with GFP or UBQLN4.GFP using GFP-Trap beads. Immune complexes were obtained from lysates of U2-OS cells mock-treated or treated with NCS (500 ng/ml, 1 hr).

(B) Schematic representation of the SeeSaw 2.0 reporter. A GFP ORF is flanked by two truncated parts of an RFP ORF (RF and FP) sharing 302 bp of homologous sequence. Two I-SceI target sites in opposite orientation are present at the 3′ end of the GFP ORF. After generation of a DSB by ectopic I-SceI endonuclease, the DSB may be repaired via NHEJ and cells will retain GFP expression, or the DSB may be repaired via HRR, creating a functional RFP ORF.

(C) Schematic representation of the DR-GFP reporter. DR-GFP is composed of two differentially mutated GFP genes: the upstream repeat contains the recognition site for the I-SceI endonuclease and the downstream repeat is a 5′ and 3′ truncated *GFP* fragment. Transient expression of I-SceI leads to a DSB in the upstream *GFP* gene; DSB repair by HRR results in GFP positive cells.

(D and E) A total number of 2000 cells/well was counted and the number of RPA70 nuclear foci (D) and 53BP1 nuclear foci (E) were quantified according to cell cycle stage and normalized to respective γH2AX foci count. High content screening kinetic experiments were analyzed with R using ordinary two-way ANOVA. Bonferroni's post hoc analysis was applied to determine p values of selected pairs defined in a contrast matrix using the R library multcomp. Error bars represent the standard deviation of the mean of 3 replicate wells analyzed in one experiment. Each experiment was carried out twice. $p < 0.05$ (*); $p < 0.01$ (**); $p < 0.001$ (***).

(F) DMFs with the indicated genotypes were pulse-chased with cycloheximide (100 μg/ml) and treated with 500 ng/ml of NCS. Cells were then fractioned at the indicated time points and the chromatin fraction was immunoblotted against MRE11. Histone H3 served as a marker for the chromatin fraction.

(G) Quantification of 6 independent experiments performed in (F). Paired t test was used for statistical analysis. $p < 0.05$ (*).

(H) Cell cycle analysis of either untreated or NCS-treated (500 ng/ml) cells with indicated genotypes between 0 and 48 hr. The distributions shown were derived from 5 independent experiments (Rep1-5). Of note, the rescue (UBQLN4^{wt}-complemented patient cells) was performed in 3 of these experiments.

(I) Cells with the indicated genotypes were pre-treated with MG132 (10μM) 1 hr prior to NCS (500 ng/ml) treatment and stained for nuclear foci of ubiquitin (Ub) at the indicated time points. 2500 cells/well were counted at each time point and Ub fluorescence was quantified using high content screening kinetic experiments, which were analyzed with R using ordinary two-way ANOVA. Bonferroni's post hoc analysis was applied to determine p values of selected pairs defined in a contrast matrix using the R library multcomp. Error bars represent the standard deviation of the mean for 3 replicate wells analyzed in three independent experiments. Not significant (n.s.) $p > 0.05$.

(J) Immunoblot of FLAG.MRE11 or empty-vector FLAG that co-precipitated with His-Ubiquitin (Ub) using Ni-NTA metal beads in whole cell lysate. Immune complexes were obtained from lysates of HEK293FT cells mock-treated or treated with NCS (500 ng/ml, 1 hr).

(K) Immunoblot of FLAG.MRE11 that co-precipitated with GFP.UBQLN4 or empty vector.GFP using GFP-beads. Immune complexes were obtained from lysates of HEK293FT cells treated with NCS (500 ng/ml, 1 hr). USP2 (50 nM) was added for 30 min at 37°C to the agarose-beads after washing of beads was completed.

(L) Representative images of MRE11 nuclear staining and ubiquitin (Ub) nuclear staining obtained 24 hr after NCS (500 ng/ml) +/− MG132 treatment using quantitative HCS microscopy. DAPI stained cell nuclei were automatically identified and assigned to a mask. Scale bars, 100 μm.

(M and N) Cells with the indicated genotypes were mock- or pre-treated with MG132 (10μM) 1 h prior to NCS (500 ng/ml) treatment and stained for nuclear intensity of ubiquitin (Ub) (M) and nuclear MRE11 intensity (N) at the indicated time points. 2500 cells/well were counted at each time point and Ub and MRE11 nuclear fluorescence was quantified using high content screening kinetic experiments. Error bars represent the standard deviation of the mean for 3 replicate wells analyzed in three independent experiments. $p < 0.05$ (*).

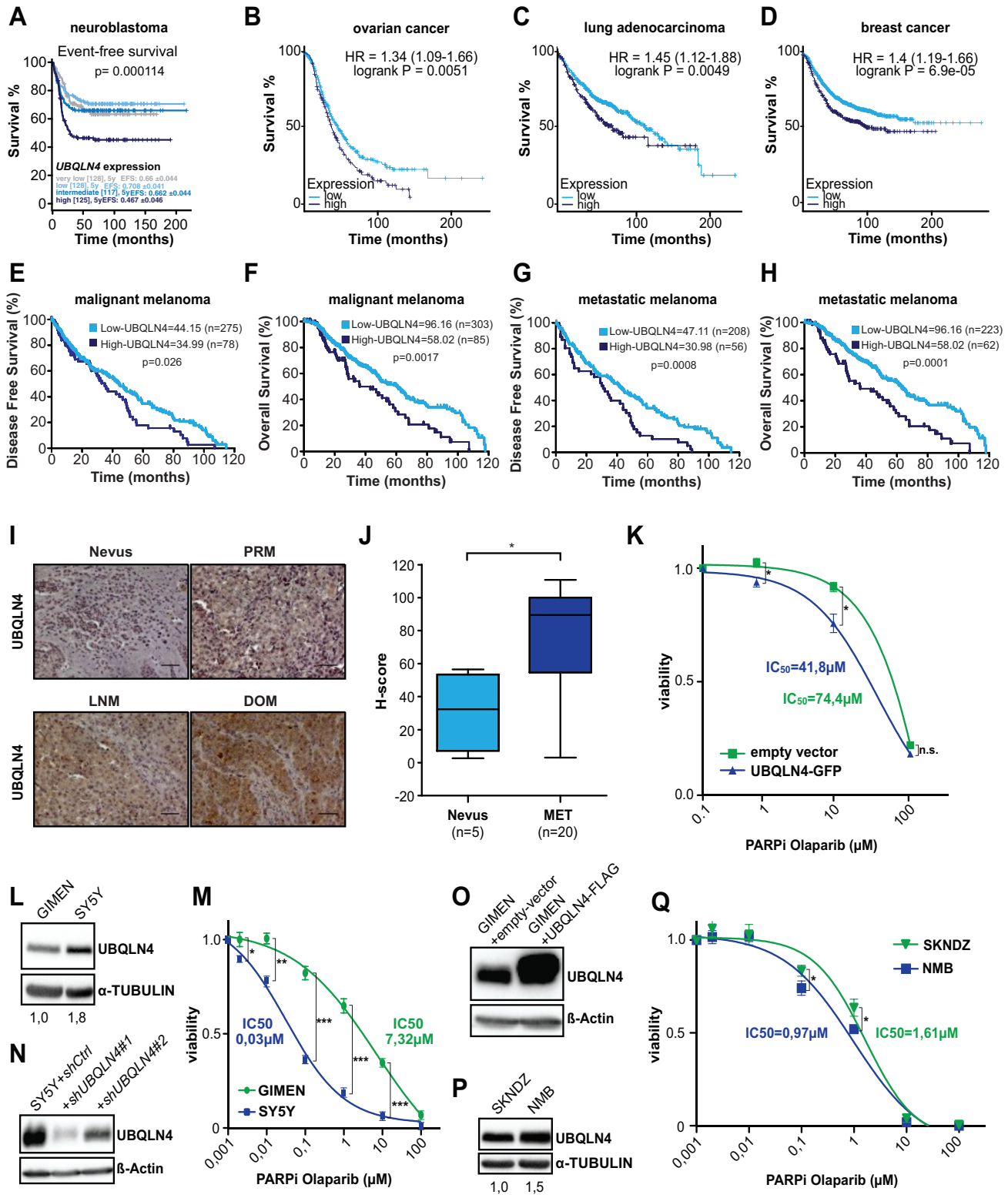

Figure S6. High-Level UBQLN4 Expression Is Associated with Aggressive Tumors that Display an Actionable PARP1 Inhibitor Sensitivity, Related to Figure 6

(A) 498 neuroblastoma cases where divided into quartiles according to the expression levels of *UBQLN4*: high (125 patients); intermediate (117 patients); low (128 patients) and very low (128 patients) expression. Kaplan–Meier curves show Event-free survival in all four subgroups.

(legend continued on next page)

(B–D) Overall Survival curve in ovarian cancer (n = 1,816, (B), lung adenocarcinoma (n = 2,437, (C) and breast cancer (n = 5,143, (D) according to either high or low *UBQLN4* mRNA expression levels. The analysis was based on publicly available datasets (Szász et al., 2016).
(E) Disease Free Survival in malignant melanoma according to high or low *UBQLN4* mRNA expression levels (mRNA z-score ≥ 2 and ≤ -2 or amplified).
(F) Overall Survival in malignant melanoma according to high or low *UBQLN4* mRNA expression levels.
(G) Disease Free Survival in metastatic malignant melanoma according to high or low *UBQLN4* mRNA expression levels.
(H) Overall Survival in metastatic malignant melanoma according to high or low *UBQLN4* mRNA expression levels. The analysis of E-H was performed on the TCGA dataset.
(I) Representative images of immunohistochemistry performed with an anti-UBQLN4 antibody in nevus, primary melanoma (PRM), lymph node metastasis melanoma (LNM), and distant organ metastasis melanoma (DOM). Scale bars, 50 μm.
(J) Quantification and comparison of UBQLN4 expression utilizing H-score staining of nevus (n = 5) and metastatic tumor samples (LNM and DOM; n = 20). Error bars represent the standard deviation. Unpaired t test was used for statistical analysis. $p < 0.05$ (*).
(K) Intracellular ATP was measured as a surrogate marker for cell viability. U2-OS cells were transduced with either empty.GFP or UBQLN4.GFP and treated with the PARP1 inhibitor olaparib for 96 hr, before ATP levels were measured using the CellTiter-Glo® Luminescent Cell Viability Assay (Promega, Germany). Error bars represent the standard deviation of the mean of 3 replicate wells analyzed in three independent experiments. p values were calculated using the t test with Welch's correction not assuming equal variance. $p < 0.05$ (*).
(L) Immunoblot depicting the level of endogenous UBQLN4 in neuroblastoma cell lines GIMEN and SY5Y.
(M) Cellular viability was assessed in neuroblastoma cell lines GIMEN and SY5Y after treatment with the PARP1 inhibitor olaparib for 96 hr. Error bars represent the standard deviation of the mean of 3 replicate wells analyzed in three independent experiments. p values were calculated using the t test with Welch's correction not assuming equal variance. $p < 0.05$ (*); $p < 0.01$ (**); $p < 0.001$ (***).
(N) Immunoblot depicting the level of UBQLN4 in neuroblastoma cell line SY5Y transduced with either *shCtrl* or two independent shRNA's targeting *UBQLN4*.
(O) Immunoblot depicting the level of UBQLN4 in neuroblastoma cell line GIMEN transduced with either empty-vector FLAG plasmid or FLAG-tagged UBQLN4.
(P) Immunoblot depicting the level of endogenous UBQLN4 in neuroblastoma cell lines SKNDZ and NMB.
(Q) Cellular viability was assessed in neuroblastoma cell lines SKNDZ and NMB after treatment with the PARP1 inhibitor olaparib for 96 hr. Error bars represent the standard deviation of the mean of 3 replicate wells analyzed in three independent experiments. p values were calculated using the t test with Welch's correction not assuming equal variance. $p < 0.05$ (*).